

Charles University in Prague

Faculty of Science

Department of Inorganic Chemistry

**Organized Nanostructured TiO₂ Materials:
Synthesis, Characterization, Applications**

PhD Thesis

Markéta Zúkalová

Prague, 2008

Prohlášení

Prohlašuji, že jsem tuto disertační práci ani její část nepředložila k získání jiného nebo stejného akademického titulu a že jsem ocitovala veškeré použité literární zdroje.

RNDr. Markéta Zukalová

V Praze dne 12. 2. 2008

Prohlášení spoluautorů

Jménem svým i ostatních spoluautorů prohlašuji, že podíl Markéty Zukalové na společných publikacích je minimálně roven alikvotnímu podílu připadajícímu na každého z autorů.

Prof. RNDr. Ladislav KAVAN, DSc.

V Praze dne 12. 2. 2008

Preamble: ORGANIZATION OF THE THESIS

This PhD thesis is based on publications (1-12) which are attached *in-extenso* at the end of this text. They make an integral part of the thesis, i.e. the text below is considered just a general introduction into the subject, as well as an extended summary of the mentioned papers. Additionally, this entrance text is upgraded by new, so far unpublished data, wherever they are relevant to the subject of the thesis. In particular, this concerns the novel solar test data on mesoporous TiO₂ films composed of up to 10 layers (Table II.3.2.1). In addition to this some recent results are attached. They deal with solar tests performed on novel kind of TiO₂ material, nanofibrous anatase prepared by means of electrospinning from the polymer solution containing a titanium dioxide precursor. The fibers were combined with mesoporous TiO₂. The fibrous, as-made product contains 20% of TiO₂ and 80% of the polymer, which is finally removed by calcination. The first measurements on this material confirmed its large application potential for dye sensitized solar cells. The fibrous TiO₂ in the bottom layer of the electrode composite is able to transport generated electrons to the current collector faster than commonly used nanoanatase and at the same time the upper layer consisting of mesoporous TiO₂ provides sufficient surface area for a dye adsorption.

I. GENERAL OVERVIEW

I.1. Titanium dioxide

Titanium dioxide was discovered in 1791 by the British amateur chemist Willem Gregor. He used a magnet to extract the mineral ilmenite (FeTiO₃) from the sand of the local river, and treated it with hydrochloric acid to remove the iron¹³. The residue was the rutile form of TiO₂. The industrial production of TiO₂ started after the First World War in 1918, when it replaced the toxic and unstable lead oxides as a white pigment in paint industry. Initially, the anatase form was used for paints, but was later replaced by rutile be-

cause of its superior optical properties. Since then, TiO_2 has remained the most important white pigment.

Titanium is the 9th most abundant element on the Earth, and comprises 0.63% of the Earth's crust¹³. Pure titanium dioxide does not occur in nature but is derived from ilmenite or leucocene ores. It is also readily mined in one of the purest forms, rutile beach sand. Ilmenite is converted to TiO_2 by the sulfate or chloride process. In the first case, sulfuric acid reacts with the mineral to form water-soluble sulfates of titanium and iron. After extraction of the iron sulfates, titanium dioxide is formed by calcination. In the chloride process, mineral rutile is treated with chlorine to form titanium tetrachloride (TiCl_4), a colorless liquid. After purification, the TiCl_4 is converted in a reaction with oxygen at elevated temperature to form high-purity TiO_2 and Cl_2 .

Crystal structure

Several TiO_2 polymorphs have been identified or proposed to exist under varying physical conditions¹⁴. Rutile, anatase, and brookite are well known naturally occurring polymorphs, and to this group Banfield et al¹⁵ added $\text{TiO}_2(\text{B})$ as the fourth naturally occurring modification. The mineral is found in weathering rims on tektites and perovskite and as lamellae in anatase from hydrothermal veins and has a density lower than that of the other three polymorphs. Among these, rutile has been generally regarded as the stable polymorph under ambient conditions, with anatase, brookite, and $\text{TiO}_2(\text{B})$ being metastable modifications¹⁶. Two more metastable modifications obtained in ambient pressure synthesis are hollandite-structured $\text{TiO}_2(\text{H})$ ¹⁷ and ramsdellite-structured $\text{TiO}_2(\text{R})$ ¹⁸. In addition to the low-pressure phases, a number of high-pressure polymorphs has been identified experimentally or suggested from theoretical calculations. These high-pressure phases have known crystal structures, and depending on the pressure, TiO_2 adopts a structure isotypic with that of one of the following compounds: orthorhombic PbO_2 (columbite-type), baddeleyite (ZrO_2), cottunite (PbCl_2), pyrite (FeS_2), or fluorite (CaF_2). The cottunite-structured TiO_2 ¹⁹ has been denoted as the hardest known oxide, with the hardness

approaching that of diamond. The columbite-type TiO_2 , referred to as $\text{TiO}_2\text{-II}$, was first characterized by Bendeliani et al¹³ in samples quenched from 4-12 GPa and 400-1500°C. $\text{TiO}_2\text{-II}$ can be prepared from anatase, rutile or brookite in the pressure range 5-12 GPa and also at ambient pressures as a metastable phase by acid dissolution of Ti_3O_5 . At pressures higher than about 12 GPa, TiO_2 adopts the monoclinic baddeleyite structure^{20,21}.

So far, practical applications have been limited to the anatase and rutile forms, which are most easily produced and seemed to have the most interesting properties. Rutile is the thermodynamically stable structure for crystallites with particle size larger than ca. 10 nm. It can be obtained by heating other polymorphs to high temperatures (700 to 1000°C). Anatase is generally formed by chemical reactions at temperatures below 500°C. Recently, new prospects of monoclinic $\text{TiO}_2(\text{B})$ applicability have been reported, based on either its fibrous morphology or special electrochemical behavior⁷. High electrochemical charge storage capacity and higher rate capability of $\text{TiO}_2(\text{B})$ resulting from its open structure and one dimensional morphology predetermine its promising application in Li-ion battery industry.

The crystal structures of anatase and rutile are based on a tetragonal symmetry, in which the Ti^{4+} ions are 6-fold coordinated to oxygen¹³. The principle difference between both structures is the arrangement of the oxygen ions. The rutile structure (space group $P4_2/mmm$) is based on a slightly distorted hexagonal close packing of oxygen ions, whereas the oxygen sub-lattice in anatase (space group $I4_1/amd$) is near cubic close packed. Both structures have edge-sharing TiO_6 octahedra, with two and four edges shared in rutile and anatase, respectively. Furthermore, the octahedra in anatase are slightly more distorted than in rutile. Orthorhombic brookite (space group $Pbca$) is of a lower symmetry, its short-range order is less regular, in brookite all six nearest-neighbor Ti-O bond lengths are different. The crystal structure of $\text{TiO}_2(\text{B})$ was determined by Marchand et al¹⁶. $\text{TiO}_2(\text{B})$ has monoclinic unit cell (space group $C2/m$). The structure is isotypic to that of Na_xTiO_2 (bronze), $x \sim 0.2$, where the name “ $\text{TiO}_2(\text{B})$ ” comes from⁷. The structure of $\text{TiO}_2(\text{B})$ is characterized by two edge-sharing TiO_6 octahedra which are linked to the

neighboring doublet of octahedra by corners. Heating at temperatures higher than 550°C under atmospheric pressure causes slow transformation of TiO₂(B) to anatase⁷.

Electronic structure

Titanium in TiO₂ having donated its 3d and 4s valence electrons to the oxygen 2p orbitals has empty d band¹³. TiO₂ is a wide-band-gap semiconductor, the band gap energy is 3.03 eV for rutile and 3.18 eV for anatase. Titanium dioxide, both natural and synthetic is usually slightly oxygen-deficient, TiO_{2-x} (x ≈ 0.01). This small oxygen deficiency, which can also be considered as Ti³⁺ impurity, provides n-type doping to the semiconductor material. Consequently, as an n-type semiconductor, it acts as a photoanode in an electrochemical cell upon photoexcitation across the band gap. The electronic structure of TiO₂(B) was calculated by Nuspl et al²². TiO₂(B) is a semiconductor with a band gap of 3 - 3.2 eV. Similar to anatase and rutile, also the n-doped TiO₂(B) shows photoanodic and photocatalytic^{23,24} activity in UV light. The photocatalytic activity may be even superior to that of Degussa P25^{23,24}, the material considered to be all purpose photocatalyst with excellent performance. The unique properties of this Degussa product arise from its special composition; it is actually mixture of anatase and rutile, while the rutile content is about 30%.

Applications

Titania has relatively high refractive index and other favorable optical properties to be used as a white pigment. Its value determines the opacity that the material confers to the matrix in which the pigment is housed. Hence, with its high refractive index, relatively low levels of titania pigment are required to achieve a white opaque coating. Therefore, it is widely used in paints and coatings (including glazes and enamels), plastics, paper, inks, fibers, food and cosmetics. One of the major advantages of the material for exposed applications is its resistance to discoloration under UV light.

Titania acts as an electrode material for dye sensitized photoelectrochemical cells. This device is based on charge injection from photoexcited organic or organometallic dye which is adsorbed on the TiO₂ surface.

Even in mildly reducing atmospheres titania tends to lose oxygen and become sub stoichiometric. In this form the material becomes an n-type semiconductor and the electrical resistivity of the material can be correlated to the oxygen content of the atmosphere to which it is exposed. Hence titania can be used to sense the amount of oxygen (or reducing species) present in an atmosphere.

The photocatalytic activity of titania results in thin coatings of the material exhibiting self cleaning and disinfecting properties under exposure to UV radiation^{25,26}. These properties make the material a candidate for applications such as medical devices, food preparation surfaces, air conditioning filters, and sanitaryware surfaces.

Titanium dioxide can electrochemically accommodate Li⁺ which is useful for a design of new Li-ion batteries. Whereas the charge storage in anatase or rutile is based on the diffusion-controlled Li-insertion into the bulk crystal, the monoclinic TiO₂(B) exhibits an unusual pseudocapacitive Li-storage mechanism⁷. Due to its open structure, TiO₂(B) accommodates hydrogen via electrochemical reduction of inserted protons, and this hydrogen can be extracted photoelectrochemically in visible light²⁷.

I.2. Spinel Li₄Ti₅O₁₂

Spinel oxides Li_{1+x}Ti_{2-x}O₄; 0 ≤ x ≤ 1/3 (space group *Fd3m*) were described in 1971 by Deschanvres et al²⁸, and electrochemically characterized in the early 1990s by Dahn, Thackeray, and Ohzuku et al²⁹. The cubic lattice constant, *a* scales with composition (*x*) according to Eq. I.2.1 (for *a* in nm)

$$a = 0.8405 - 0.0143x \quad (\text{I.2.1})$$

The end members of the series, *i.e.*, LiTi_2O_4 and $\text{Li}_{4/3}\text{Ti}_{5/3}\text{O}_4$ ($\text{Li}_4\text{Ti}_5\text{O}_{12}$) are metallic (superconducting below 11 K) and semiconducting, respectively. Both materials exhibit similar Li-insertion electrochemistry, the formal potential (vs. Li/Li^+ reference electrode) of Li insertion being (1.36-1.338) V for LiTi_2O_4 and (1.55-1.562) V for $\text{Li}_4\text{Ti}_5\text{O}_{12}$, respectively.

$\text{Li}_4\text{Ti}_5\text{O}_{12}$ accommodates Li with a theoretical capacity of 175 mAh/g (based on the mass of the starting host material) according to the equation



The spinel host structure accommodates Li^+ without significant changes of lattice constants, hence, it is called “zero strain material”. Consequently, these materials show excellent cycle life, and Li^+ diffusion coefficients of about $10^{-6} \text{ cm}^2/\text{s}$ (from neutron radiography) or $2 \cdot 10^{-8} \text{ cm}^2/\text{s}$ (from electrochemistry) have been reported⁴.

Applications

A promising application of spinel $\text{Li}_4\text{Ti}_5\text{O}_{12}$ is as an anode material for lithium ion batteries or hybrid capacitance/insertion devices. The $\text{Li}_4\text{Ti}_5\text{O}_{12}$ electrode provides outstanding structural stability for many hundreds of cycles. The excellent structural and chemical stability of $\text{Li}_4\text{Ti}_5\text{O}_{12}$ under the working conditions of the cell represent characteristics of an ideal insertion electrode. Because of its relatively low voltage vs lithium, $\text{Li}_4\text{Ti}_5\text{O}_{12}$ is not used as a positive electrode in practical lithium cells; this compound is of greater interest as a negative electrode because it is safe compared to metallic lithium or graphite intercalation compounds, and because it can be coupled with “4 V” positive electrodes such as LiCoO_2 , olivines LiMPO_4 (M=Fe, Mn) and LiMn_2O_4 or “3 V” Li_xMnO_2 electrodes to provide 2.5 V and 1.5 V cells, respectively^{29-31,31}.

II. NANOCRYSTALLINE TiO₂-BASED MATERIALS: SYNTHESSES, CHARACTERIZATION, ELECTROCHEMICAL PROPERTIES

INTRODUCTION: Properties of nanocrystalline materials in general

Nanostructured materials are those with at least one dimension falling in nanometer scale, and include nanoparticles, nanorods and nanowires, thin films, and bulk materials of nanoscale building blocks or consisting of nanoscale structures. Materials in the micrometer scale exhibit physical properties identical to these of macroscopic crystals. However, materials in the nanometer size (<1 μm) may exhibit physical properties distinctively different from those of macroscopic crystals. A transition from atoms or molecules to bulk crystals takes place in this size range. The peculiar properties of nanomaterials arise from different fundamentals. For example, crystal structures stable at elevated temperatures are stable at much lower temperatures in nanometer sizes, bulk semiconductors increase their bandgap (quantum-size effect), and eventually become insulators when the characteristic dimension is sufficiently small (typically several nanometers), the huge surface energy is responsible for reduction of thermal stability³² and melting point. The phase stability of two polymorphs may be reversed because their surface energies are different. Size confinement results in a change of both electronic and optical properties of nanomaterials. Size has other implications. Small crystals grow by different pathways than big crystals³³. The crystal growth pathway that may predominate under some conditions has been described as "oriented attachment" or "oriented aggregation". In this pathway, crystals no more than a few nanometers in diameter aggregate and rotate so that adjacent surfaces share the same crystallographic orientation. The pair of adjacent interfaces are eliminated and the pair of nanoparticles are converted to a larger single crystal.

Nanocrystalline TiO₂ (anatase) has attracted considerable interest for applications in photoelectrochemical solar cells. Nanostructures are advantageous for photoelectrochemical cell devices for highly efficient conversion of light to electrical power due to its large surface area at which photoelectrochemical processes take place. Also for the application in Li-ion batteries, the nanocrystalline morphology is beneficial, especially if fast charging/discharging of a battery is requested. Obviously, there is a motivation for ex-

ploring of electrochemical properties of nanocrystals in general, and Ti(IV) oxides in particular. The impact of nanocrystalline oxide materials to Li-ion batteries is highlighted by larger charging rates due to small transport distances in the solid host³⁴. By decrease of the crystal dimensions, the solid-state Li⁺ diffusion is progressively replaced by surface-confined Li-storage, i.e. there is a natural link between batteries and supercapacitors in the area of nanosized crystals³⁴. However, ultrasmall crystals are handicapped by sluggish Li-transport^{4,35,36} and by charge irreversibility due to parasitic surface reactions⁴. Hence, there is certain optimum of crystal size for the given host material and fast Li-charging/discharging⁴.

TiO₂ nanomaterial in the Q-size domain has the electronic band gap larger than that of macroscopic crystal, which manifests itself as a blue-shifted absorption in the UV region. Its optical properties allow it to be a good candidate for UV protection applications³⁷. The photocatalytic activity of amorphous titania is negligible; that of nanocrystalline anatase is greater than that of rutile; and that of nanocrystalline rutile increases with decreasing particle size. Due to its high photocatalytic activity, stability and non-toxicity, TiO₂ represents a promising photocatalyst for the decomposition of various liquid and gaseous pollutants. TiO₂ photocatalyst can also be used to kill bacteria. Various glass products (i.e. mirrors, eyeglasses) can now be imparted with antifogging functions with TiO₂ nanomaterials having superhydrophilic or superhydrophobic effect. On extremely hydrophilic surfaces, a water droplet will completely spread (an effective contact angle of 0°). This occurs for surfaces that have a large affinity for water (including materials that adsorb water). On many hydrophilic surfaces, water droplets exhibit contact angles of 10° to 30°. The water on the superhydrophilic surface does not form droplets, just a thin transparent film. On highly hydrophobic surfaces, which are incompatible with water, one observes a large contact angle (70° to 90°). Some surfaces have water contact angles as high as 150° or even nearly 180°. On these surfaces, water droplets simply rest on the surface, without actually wetting to any significant extent. These surfaces are termed superhydrophobic.

II.1. SYNTHESSES OF MATERIALS

II.1.1. Aluminum - stabilized anatase TiO₂

The $\text{Al}_{13}\text{O}_4(\text{OH}_{24})^{7+}$ solution (0.12 mol/L) was prepared by dissolving 13.1338 g of $\text{AlCl}_3 \cdot 6\text{H}_2\text{O}$ in 420 ml of water, and the pH was adjusted to 3.95 with concentrated ammonium hydroxide. This solution was slowly added to a solution of $(\text{NH}_4)_2\text{Ti}(\text{OH})_2(\text{C}_3\text{H}_2\text{O}_3)_2$ (Tyzor LA, DuPont) and cetyltrimethylammonium chloride (CTAC, Lonza) as described below.

Sample A: 8.27 g of Tyzor (15.2 mmol Ti) and 8.82 g of CTAC solution (8 mmol) were combined. 6.62 ml (0.8 mmol) of the above described aluminum solution was diluted to 80 ml with water, and then was slowly added to the Tyzor/CTAC mixture at vigorous stirring.

Sample B: 6.82 g of Tyzor (12 mmol Ti) and 8.82 g of CTAC solution (8 mmol) were combined. 33.09 ml (4 mmol) of the above described aluminum solution was diluted to 80 ml with water, and then was slowly added to the Tyzor/CTAC mixture at vigorous stirring.

Sample C: 4.54 g of Tyzor (8 mmol Ti) and 8.82 g of CTAC solution (8 mmol) were combined. 66.18 ml (8 mmol) of the above described aluminum solution was diluted to 80 ml with water, and then was slowly added to the Tyzor/CTAC mixture at vigorous stirring.

II.1.2. Organized mesoporous TiO₂ films

Titania films were grown from stock solution made by the slow addition of 9.7 g of concentrated HCl (Aldrich) to 12.7 g of titanium ethoxide (Aldrich) under vigorous stirring. Separately, 4.0 g of block copolymer Pluronic P123 $(\text{OH}(\text{CH}_2\text{CH}_2\text{O})_{20}(\text{CH}_2\text{CH}(\text{CH}_3)\text{O})_{70}(\text{CH}_2\text{CH}_2\text{O})_{20}\text{H})$, (BASF) was dissolved in 36.3 g of 1-butanol (Aldrich) and then added to the HCl/Ti(EtO)₄ solution. This solution was aged with stirring at ambient temperature for at least 3 hours. The films were deposited onto F-doped SnO₂ conducting glass (TEC 8 from Libbey-Owens-Ford, 8 Ω/square) and 7.5 cm

x 2.5 cm² sized slides of soda-lime-silica glass. The dip coating was carried out at the withdrawal rate of 0.8 mm/s. The green layer was aged at about 75% relative humidity and temperature 24 – 25 °C for 30 hours. Subsequently, the layer was calcined in air at 350 °C for 2 hours (heating rate: 1 °C/min). For the preparation of thicker films consisting of more layers, the described procedure was repeated.

II.1.3. Anatase inverse opal

Thin-film electrodes were fabricated with the aid of a latex template film on conducting glass electrode (F-doped SnO₂, TEC 8 from Libbey-Owens-Ford, 8 Ω/square). The conducting glass was cleaned by sonication in methanol, water and finally by the ozone UV cleaner (Jelight Co., Inc). The layer of latex template was grown by evaporation according to Ref. ⁶ as follows: Aqueous suspension (0.1 wt%) of monodisperse, carboxylate-modified polystyrene latex spheres (Seradyn Co.) was sonicated for 30 min. (The purchased suspension of latex spheres was diluted by ultrapure deionized water (Milli-Q System, Millipore), 18 MΩ.cm.) The latex film was grown on vertically positioned conductive glass by complete evaporation of this suspension at 60 °C during 2 days. The template layer was reasonably uniform, ca. 3 μm thick (alpha-step profilometer, Tencor Instruments). The voids in the opal template layer on conducting glass were filled by three different methods (electrodeposition, liquid-phase deposition and vapor-phase deposition) as specified below. Finally the latex template was removed by calcination at 450°C during 30 min. The three methods of titania deposition in the voids of latex template were as follows: (1) Electrochemical deposition from 50 mM aqueous solution of TiCl₃, pH 2.4 by galvanostatic oxidation at 10 μA/cm² for 10 hours³⁸, (2) Liquid phase deposition from a mixture of 0.2 M (NH₄)₂TiF₆ + 0.3 M H₃BO₃, pH 3, adjusted by HCl. The solutions of (NH₄)₂TiF₆ and H₃BO₃ were prepared separately and mixed only before application. The reaction was carried out at 60°C during 30 min³⁹⁻⁴¹. (3) Deposition from a vapor phase: the glass-supported template layer was exposed to vapor of titanium(IV) tetraisopropoxide at 100°C for 10 min⁴². For the methods ad 1 and 2, also blank (non-templated) layers were prepared. The synthetic protocol was identical, except the layer was deposited on bare conducting glass, without any latex template.

The inverse opal powder was prepared according to a modified protocol^{43,44}. The solution of latex particles in water (4.5vol.%, 500 nm in diameter, provided by the Max Planck Institute of Colloids and Interfaces, Germany) was centrifuged at 4000 rpm for 26 hours. After drying at ambient temperature, 1 g of the template was disintegrated into lumps and soaked with 2-propanol. Subsequently 20 ml of titanium(IV) isopropoxide was added drop wise and the mixture was filtered on a Buechner funnel. The composite was dried in air and then under vacuum at room temperature for 7 hours and annealed at 575°C for 2.5 hours under air flow (heating rate 5°C/min). The final product was flakey powder with a typical opal-like iridescence.

II.1.4. Nanostructured TiO₂(B)

The precursor, X-ray amorphous TiO₂, was prepared by precipitation of the aqueous solution of K₂TiF₆ (Aldrich) with ammonium hydroxide solution (25wt.%, Fluka). The product was washed with H₂O and dried, S_{BET} = 584 m²/g. Alternatively, the amorphous TiO₂ (S_{BET} = 518 m²/g) was prepared by hydrolysis of titanium isopropoxide at 0°C as described elsewhere⁴⁵.

Sample A: 10 g of amorphous TiO₂ was mixed with 7.78 g of Cs₂CO₃ (Aldrich) and mortared carefully. The mixture was then decarbonated at 800°C for 4 h, mortared again and annealed at 800°C in a crucible with a tight lid for 24 h, twice, with grinding at the interval. The product was then mortared, and ion-exchanged with 1 M HCl (100 mL per 1 g of product) for 4 x 24 h at vigorous stirring with the fresh acid exchanged every 24 h. The dried sample was finally calcined at 500°C for 1 h. The product contained <10 ppm K (according to ICP analysis; obviously residuum of the parent solution adsorbed on amorphous TiO₂ surface; see above) and its surface area was S_{BET} = 29.5 m²/g.

Sample B: This material was prepared according to the original synthetic protocol of TiO₂(B)¹⁶. An intimate mixture of 20 g KNO₃ (Aldrich) and 31.6 g of TiO₂ (Bayer, PKP04090) was annealed at 1000°C for 2 days. The product was mortared and hydrolyzed with 0.4 N HNO₃ (100 mL of HNO₃ per 1 g of product) for 3 days at vigorous stirring with the fresh acid every 24 h. The sample was dried in air at ambient temperature,

then under vacuum overnight and calcined at 500°C for 30 min. The final product contained 120 ppm K (according to ICP analysis) and its surface area was $S_{\text{BET}} = 9.9 \text{ m}^2/\text{g}$.

Sample C: 3.5g of amorphous TiO_2 was autoclaved in 100 mL of 10 M NaOH at 250°C for 48 h, then washed with H_2O and autoclaved in 0.1 M HNO_3 at 200°C for 2.5 h. The dried sample was then calcined at 500°C for 1 h. The surface area of the product was 34.7 m^2/g .

II.1.5. Nanocrystalline spinel $\text{Li}_4\text{Ti}_5\text{O}_{12}$

1-1.8 M solution of lithium ethoxide (Aldrich) in absolute ethanol was mixed with a stoichiometric amount (4/5) of titanium (IV) isopropoxide (Aldrich) or titanium (IV) n-butoxide, (Aldrich). The solution was hydrolyzed by water, and concentrated on rotary evaporator (40°C, 20 mbar) to a concentration of 10-20 wt%. (Sometimes, this slurry was autoclaved at 150°C for 10 hours, in order to achieve the growth of particles). Polyethylene glycol (molecular weight 20 000, Merck) was added in the proportion of 100-150 % of the weight of $\text{Li}_4\text{Ti}_5\text{O}_{12}$, and the mixture was stirred overnight. A proprietary calcination program was developed to minimize the anatase impurities.

II.2. METHODS

Electrode preparation

Powder sample was dispersed in aqueous medium into viscous paste according to the previously developed methods^{38,46,47}. The powder (0.3 g) was mixed under stirring or gentle mortaring with 0.8 mL of 10 % aqueous solution of acetylacetone. Subsequently, 0.8 mL of 4 % aqueous solution of hydroxypropylcellulose (Aldrich, MW 100,000) was added and finally 0.4 mL of 10 % aqueous solution of Triton-X100 (Fluka). Before use, the prepared slurry was homogenized by stirring. If the slurry was too viscous, it was further diluted by water. Titanium grid (5 x 15 mm, Goodfellow) was used as the electrode support for Li insertion tests. Electrodes were prepared by dip-coating, the coated area was ca. 5 x 5 mm^2 . The prepared electrodes were dried in air, and finally calcined in air at 450 °C for 30 min. The amount of active electrode material was from 0.2 to 0.7 mg.

Blank experiments confirmed that a bare Ti grid had negligible electrochemical charge capacity compared to that of the active material. Alternatively, the slurry was also deposited on a sheet of conducting glass (F-doped SnO₂, TEC 8 from Libbey-Owens-Ford, 8 Ω/square) using a doctor-blading technique⁴⁷. These electrodes served primarily for photoelectrochemical measurements. However, they are also applicable for dark electrochemistry tests, such as Li insertion. The sheet of conducting glass had dimensions: 3 x 5 x 0.3 cm³. A Scotch-tape at both edges of the support (0.5 cm) defined the film thickness and left part of the support uncovered for electrical contact. The film was finally calcined for 30 min in air at 450°C. After cooling down to room temperature, the sheet was cut into ten electrodes 1.5 x 1 cm² in size; the geometric area of the TiO₂ film was 1 x 1 cm².

Dye sensitized solar cell preparation

The TiO₂ thin film on glass support covered with conducting layer (FTO – F doped SnO₂) was scraped leaving an area of about 0.5 x 0.5 cm², then dipped in the solution of either the N719 or N945 dye (see part II.3.2.). The dipping time was 42 hours in all experiments. After withdrawal, the layer was washed with acetonitrile, dried in dry air at ambient temperature and closed with the Surlyn tape separating it from the counterelectrode (Pt on a glass support). Finally, the cell was filled with an electrolyte through a hole in the counterelectrode and sealed. The electrolyte solution was 0.6 M N-methyl-N-butyl imidazolium iodide, 40 mM I₂, 0.075 M lithium iodide, 0.26 M tert-butylpyridine, 0.05 M guanidine thiocyanate in acetonitrile/valeronitrile (85/15, v/v). The ends of both electrodes were covered with Al to improve the contact. The cell active area was defined by a mask.

Characterization

XRD – Powder X-ray diffraction (XRD) was studied with Siemens 5000 and Bruker D-8 Advance using Cu K α radiation.

Adsorption isotherms of nitrogen and krypton at 77 K were measured with a Micromeritics ASAP 2020 instrument. Before the adsorption measurement, all samples were de-

gassed at 523 K overnight. The BET surface areas were calculated using the data in the range of relative pressure p/p_0 from 0.05 to 0.25.

SEM – Scanning electron microscopy images were obtained at Hitachi FE SEM S-4800 and JEOL JSM-03 microscopes.

TEM – Transmission electron microscopy images were taken by Tecnai F30 and JEOL JEM 3010 microscopes.

Cyclic voltammetry of Li⁺ insertion, chronoamperometry – (Autolab PGSTAT 30 Ecochemie) potentiostat controlled by a GPES - 4 software. The reference and auxiliary electrodes were from Li metal; hence, potentials are referred to the Li/Li⁺ (1M) reference electrode. LiN(CF₃SO₂)₂ (Fluorad HQ 115 from 3M) was dried at 130°C/1 mPa. Ethylene carbonate (EC) and 1,2 - dimethoxyethane (DME) were dried over the 4A molecular sieve (Union Carbide). The electrolyte solution 1 M LiN(CF₃SO₂)₂ + EC/DME (1/1 by volume) contained 10-15 ppm H₂O as determined by Karl Fischer titration (Metrohm 684 coulometer). All operations were done under argon in a glove box.

Profilometry (layer thickness) was measured by alpha-step profilometer (Tencor Instruments).

ICP – inductively coupled plasma analyser (Ecochem)

Photoelectrochemistry - the light source was a 450 W xenon lamp that was focused to give light power of 1000 W/m², the equivalent of one Sun at AM 1.5, at the surface of test cell. The spectral output of the lamp was matched in the wavelength region of 340-800 nm with the aid of a Schott KG-5 sunlight filter. This reduced the mismatch between the simulated and the true solar spectrum to less than 2%. The differing intensities were regulated with neutral wire mesh attenuator. The applied potential and cell current were measured using a Keithley model 2400 digital source meter.

Raman spectra were excited by Ar⁺ laser at 2.41 eV (Innova 305, Coherent) and recorded on a T-64000 spectrometer (Instruments, SA)

Photocatalytic measurements

The photoreactor was mounted into the experimental set-up consisting of the gas supply, the reaction and the analytic systems. The gas supply was realized with commercially available gas bulbs (Linde AG, Leuna). The flow rates of the gases were adjusted by flow meters (Bronkhorst AB, Ruurlo, NL). The gases were mixed in a mixing chamber. The reactor operated as a continuous stirred tank reactor in order to avoid local concentration gradients along the flow direction in the reaction chamber. The composition of the incoming as well as that of the effluent gas was determined by a FTIR-analyser (IFS 28, Bruker, Hamburg). The temperature of the catalyst plate was adjusted by a heating plate and was controlled by a thermocouple. To eliminate adsorbed hydrocarbons, the catalyst plate was inserted in the photoreactor and irradiated for three hours in an atmosphere containing 100% oxygen. The absorbed irradiation intensity was around 180 W/m², the catalyst temperature 160°C. The photocatalytic activity of material under study was compared to the standard photocatalyst Hombifine N (anatase, surface area 300 m²/g, Sachtleben).

UV-Vis spectra were measured on Hewlett Packard 8450 diode array spectrometer.

II.3. RESULTS

CHARACTERIZATION AND ELECTROCHEMICAL PROPERTIES

II.3.1. Mesoporous electrode material from aluminum - stabilized anatase TiO₂ for lithium ion batteries

The insertion/extraction of Li to/from the TiO₂ lattice is described by the equation:



The most active form of TiO_2 for the reaction II.3.1.1 is anatase, in which the insertion coefficient, x is usually close to 0.5. The performance of nanocrystalline TiO_2 for Li-storage is significantly controlled by the particle morphology^{5,47-49} and, for instance, the TiO_2 nanosheets exhibit well distinguished charging in the supercapacitive regime⁵. This effect is traced also in mesoporous anatase made by supramolecular templating⁴⁹. Since the Li^+ insertion into some other TiO_2 polymorphs (rutile, brookite) is mostly considered to be less significant, the presence of anatase phase is essential for lithium batteries application. Synthetic strategy stems from the goal of fabrication of high-surface mesoporous titanium dioxide with well-developed anatase crystallinity at the same time. These contradictory requirements can be met by protecting of the surfactant-templated mesoporous TiO_2 framework by deliberately added inorganic component. This synthetic protocol was first demonstrated by Elder et al⁵⁰ on zirconia-stabilized TiO_2 ($\text{Zr}/\text{Ti} = 1/3$), called PNNL-1. There are various examples of advanced materials based on the titania/alumina system. Aluminum was found to be crucial for stabilization of the anatase lattice during chemical transport reactions in the $\text{TiO}_2\text{-TeCl}_4$ system, and large anatase single crystal could only be synthesized with the aid of Al-stabilization⁵¹. A special form of mesoporous alumina has been frequently used as a template for the fabrication of anatase nanotubes and nanowires⁵²⁻⁵⁶. Zhang and Banfield⁵⁷ reported that the anatase-to-rutile phase transformation is retarded to higher temperatures with the addition of Al_2O_3 to anatase TiO_2 .

Mesoporous Al-stabilized TiO_2 (anatase) exhibits unique core (anatase)/shell (rutile) structure, which can be traced only by micro-Raman spectroscopy, but not by X-ray diffraction or Li-insertion electrochemistry. The prepared materials exhibit considerable increase of surface area with the Al-content. The mesopore volume increases in the same series, but the mesopore diameter is roughly uniform (from 2.4 to 2.6 nm, see Tab. II.3.1.1)¹. The largest Li-storage capacity close to $x = 0.5$ was determined for the sample B (see II.1.1.) from cyclic voltammetry of Li- insertion. Since the voltammetric response of alumina is dominated by capacitive charging only, its presence may decrease the overall Li-insertion capacity of our materials. The small drop of Li-storage capacity due to

low amount of inactive alumina in the samples might be compensated by the increase of the surface area (Table II.3.1.1), which promotes the Li-accommodation on the voltammetric time scale. This provides rational for the found optimum performance of the sample B.

The cyclic voltammogram of Li-insertion into anatase can be evaluated assuming irreversible charge transfer kinetics. The standard rate constant of charge-transfer, k_0 can be determined from the peak current density I_p and peak potential, E_p according to the equation:

$$I_p = 0.227nFACk_0 \exp[-\alpha nF(E_p - E_f)/RT] \quad (\text{II.3.1.2})$$

where n is number of electrons in reaction II.3.1.1, A is electrode area (approximated by its equivalent BET surface area), F is Faraday constant, α is the charge-transfer coefficient ($\alpha \approx 0.5$), E_f is the formal potential determined for the slowest scan (0.1 mV/s in our case) and c is the maximum concentration of Li^+ (or Ti^{3+}) in the accumulation layer. Assuming the limiting composition of the insertion product to be $\text{Li}_{0.5}\text{TiO}_2$ (cf. Eq. II.3.1.1), the concentration c equals 0.024 mol/cm^3 . The rate constants of Al-stabilized anatase are comparable to the values of non-stabilized anatase (Table II.3.1.1) as well as to those of other pure anatase nanocrystals^{48,58}.

The peak current (I_p) also scales with square root of the scan rate, ν , as it is expected for diffusion-controlled irreversible kinetics^{58,59}:

$$I_p = 0.4958nFAC(D\alpha nF\nu/RT)^{1/2} \quad (\text{II.3.1.3})$$

where D is the chemical diffusion coefficient of Li^+ . Equation (II.3.1.3) can be used for the determination of D . The found values (collected in Tab. II.3.1.1) compare well to the corresponding values of nanocrystalline anatase⁵⁸ and organized mesoporous anatase⁴⁹. Diffusion coefficients determined from the electrochemical impedance spectroscopy² at low frequencies can hardly be assigned to the Li diffusion inside the ordinary anatase lat-

tice, whereas the D values at high-frequency ranges match those of nanocrystalline anatase (10^{-14} – 10^{-17} cm² s⁻¹) of different origins^{49,60}.

In general, the diffusion coefficients tend to decrease with decreasing particle size for oxidic Li-insertion hosts^{4,35,36}. This trend is not seen in our materials. Their electrochemical properties are not characterized by sole particle size, but other less-common effects, such as lattice distortion and core-shell morphology, are at play. The Al-stabilization improves Li-insertion by enhancing the active surface area, but also decreases the Li-storage capacity. Hence, the optimum materials are found for medium Al-contents.

Table II.3.1.1:

Structural and electrochemical properties of Al-doped TiO₂ samples referred to those of pure anatase¹. S_{BET} = BET surface area; V_{ME} = mesopore volume; D_{ME} = mean mesopore diameter; E_{f} = formal potential of Li-insertion; k_0 = rate constant of Li-insertion; D = chemical diffusion coefficient of Li⁺.

	Sample A	Sample B	Sample C	TiO ₂ anatase	
				Bayer ^a	BL ^b
Ti/Al (atomic)	25	11	6	∞	∞
Al ₂ O ₃ (wt%)	2.5	5.5	9.6	0	0
Crystal size (nm)	5.6	4.1	3.0	10	21
a-constant (Å)	3.7810	3.8075	3.7875	3.7760	-
c-constant (Å)	9.3807	9.3664	9.3363	9.5139	-
S_{BET} (cm ³ /g)	55	92	185	154	73
V_{ME} (cm ³ /g)	0.036	0.062	0.110	- ^c	- ^c
D_{ME} (nm)	2.6	2.7	2.4	- ^c	- ^c
E_{f} (V vs. Li/Li ⁺)	1.85	1.84	1.83	1.88	1.85
$k_0 \cdot 10^{10}$ (cm/s)	2.3	0.9	0.9	3.0	5.0
$D \cdot 10^{17}$ (cm ² /s)	5.4	6.5	6.0	3.4	4.6

^a Bayer PKP09044 (reference material of pure anatase)

^bBL = Blank synthesized as A-C (see II.1.1.), but without addition of Al-precursor

^c mesoporous ordering is not defined

II.3.2. Organized mesoporous TiO₂ films

Complex nanostructured composites made by molecular or nanoparticle assembly can lead to the production of the efficient multifunctional systems exhibiting new and improved properties through the collective behavior of the functional units⁶¹. The synergistic assembly capability of molecular organic and inorganic species has been recognized as a general and powerful approach for the fabrication of 3-D continuously ordered structures at length scales ranging from several angstroms to tens of nanometers⁶¹. The surfactant-templated synthesis of TiO₂ mesoporous molecular sieves (analogous of siliceous mesoporous molecular sieves such as MCM-41) was announced in 1995, but this work was later questioned⁶². The synthetic procedures, which appeared to be successful for mesoporous silica, usually fail for TiO₂. The reason is that the original mesoporous TiO₂/template composite easily collapses during calcination (detemplating) because of easy crystallization of titanium dioxide^{62,63}. The only exception to this rule is templating by triblock copolymers pioneered by Stucky et al⁶⁴⁻⁶⁶, which gives well organized mesoporous anatase materials upon calcination^{49,64-67}. Whereas the first synthetic efforts were directed toward silica-based materials for applications in sorption, separation and catalysis⁶¹, mesoporous/nanoporous TiO₂ has been intensively studied in the past decade. The major synthetic challenge is to introduce crystallinity into the framework while preserving the highly ordered mesostructural integrity of the material. In the method developed by the Stucky's group⁶⁴ amphiphilic poly(alkylene oxide) block copolymers were used as structure-directing agents in non-aqueous solutions for organizing the network-forming metal-oxide species. The organized mesoscopic oxide is formed through a mechanism involving block-copolymer self-assembly and complexation of the metal atom during restrained hydrolysis of the metal chloride. This seemingly trivial technique involves a complex mechanism, called evaporation-induced self-assembly⁶⁸⁻⁷⁰. Hence, the quality of produced films is crucially dependent on experimental details, such as ambient humidity and withdrawal rate⁷¹. The prepared thermally stable mesoporous oxides exhibit a robust inorganic framework with thick channel walls. In the case of TiO₂, the walls are from amorphous TiO₂, with embedded nanocrystalline anatase⁴⁹. It is interesting to note that the hydrolysis of TiCl₄ in the absence of any templates gives only the rutile phase of

TiO₂⁷². The synthetic protocol was further varied by replacing TiCl₄ with Ti(IV) tetraethoxide^{66,71,73,74} and by replacing ethanol with 1-butanol⁷³. A composite of Pluronic templated TiO₂ with regioregular poly(3-hexyl thiophene) is applicable for solid-state photo-voltaics^{71,75}, but the performance of actual cells is limited by poor hole transport⁷⁵ and incomplete filling of mesopores⁷¹. The Pluronic templated TiO₂ was also modified by CdS or CdSe nanoparticles for a liquid-junction photoelectrochemical cell^{61,76}. The sensitization of surfactant-templated TiO₂ to visible light was successfully demonstrated, but solar efficiency of this cell was not reported^{61,76}. Recently, photoanode for DSC (dye sensitized solar cell) was fabricated from worm-like TiO₂ made by Pluronic templating, but the mesoporous film was not ordered⁷⁷.

The synthesis of mesoporous TiO₂ thin films by surfactant templating⁶⁴ led to the layers of sub-micron thicknesses only. For the applications of these films in DSC, two issues must be addressed. First, the films must be highly crystalline for the transfer of the injected electrons. Secondly, the films have to reach a certain thickness. Sub-micron films provide insufficient physical surface area per unit of projected area (roughness factor; R_f). This is critical for light harvesting in DSC, which occurs just in a monolayer of the dye on TiO₂ surface⁷⁸. So, attempts to increase both the thickness and the crystallinity are highly desired.

To fabricate thicker films with larger R_f , we have implemented a simple technique of repeated layer-by-layer deposition by dip coating. By careful control of the deposition conditions we have succeeded in deposition of mechanically stable and crack-free 2.3 μm films composed of up to 10 layers. Fig. II.3.2.1. shows the top-view SEM (scanning electron microscopy) image of either 1 or 10 layers films. The surface of the 10th layer still preserves the same organized mesoporous morphology as that of the 1st one. The bulk structure of mesoporous films was explored by adsorption measurements and was confirmed not to be significantly perturbed by multiple layer deposition. Our 1 μm -thick mesoporous film made from 3 layers showed enhanced solar conversion efficiency of DSC by about 47 % compared to that of a 1 μm -thick film made from traditional non-organized nanocrystalline anatase⁹. The TiO₂ films were sensitized by two dyes: N719 =

bis(tetrabutylammonium) cis-dithiocyanatobis(2,2'-bipyridine-4-COOH,4'-COO⁻) ruthenium(II)⁷⁹ or N945 = (4,4-dicarboxy-2,2'-bipyridine)(4,4'-di-(2-(3,6-dimethoxyphenyl)ethenyl)-2,2'-bipyridine) cis-dithiocyanato ruthenium (II). To evaluate the quality of the particular electrodes, the incident photon to current conversion efficiency (*IPCE*) can be used as a testing parameter:

$$IPCE = \frac{Jhc}{\lambda P_L e} \quad (\text{II.3.2.1})$$

J is the photocurrent density, h is the Planck constant, c is the velocity of light, λ is the photon wavelength, and P_L is the monochromatic light intensity (in W/m^2). It is determined in front of the window, and is not corrected for absorption and reflection losses in the window, electrolyte solution and electrode. For a sensitized TiO_2 surface, the *IPCE* can be also expressed using the dye and substrate parameters⁵¹:

$$IPCE = \eta_{inj}(1 - 10^{-\varepsilon\Gamma}) = \eta_{inj}(1 - 10^{-\varepsilon R_f \Gamma_0}) \quad (\text{II.3.2.2})$$

η_{inj} is the quantum yield of charge injection from the photoexcited dye ($\eta_{inj} \approx 100\%$ in many practical cases), ε is the extinction coefficient, Γ is the overall surface concentration of the dye (in moles per projected electrode area, A_0). Obviously, $\Gamma = R_f \Gamma_0$, where Γ_0 is the specific surface coverage (in moles per physical electrode area, A). Although *IPCE* is useful parameter in evaluation of solar cells, a more practical criterion is the overall energy conversion efficiency for white solar light, ϕ_{sol} defined as:

$$\phi_{sol} = \frac{J_{sc} U_{oc} f}{P_{sol}} \quad (\text{II.3.2.3})$$

J_{sc} is the short circuit photocurrent density, U_{oc} is the cell open-circuit voltage, f is the fill factor and P_{sol} is the incident intensity of white solar light (in W/m^2 ; for AM 1.5 solar light $P_{sol} = 1 \text{ kW/m}^2$). The solar performance of a sensitized TiO_2 photoanode is influenced by its surface area, expressed by the roughness factor, crystallinity, porosity, quality of crystal interconnects, etc. The increase in surface area raises the amount of adsorbed

dye on the film surface, and the presence of defect-free and well interconnected anatase crystals is essential for the electron transport from the dye to the substrate current collector.

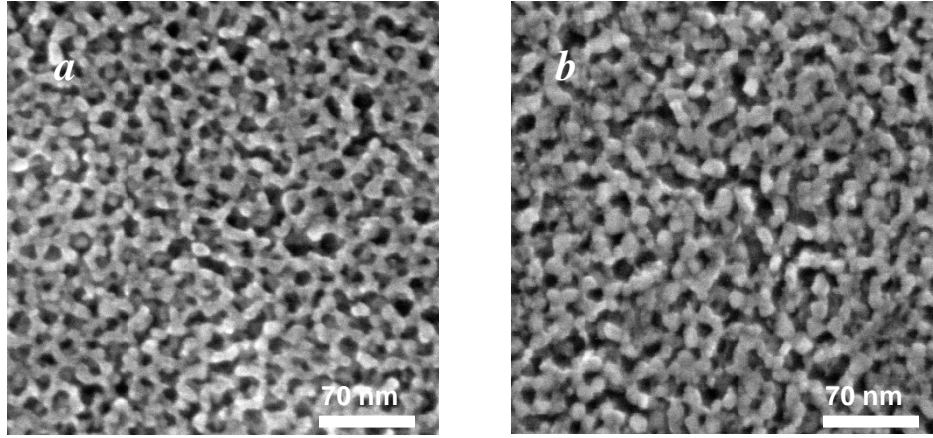


Figure II.3.2.1:

SEM images of the surface of mesoporous film made from one (a) and ten (b) successively deposited layers.

The research strategy has been based on creation of the set of representative samples to be incorporated in solar cells. To optimize the synthetic conditions of making films, the layers of different structure and thicknesses were tested in solar cells containing the N945 dye.

The results of solar cell tests¹¹ are summarized in Table II.3.2.1 for electrodes, which were sensitized with the N-945 dye. The motivation for using this dye resulted from beneficial optical parameters of N-945 compared to N-719: the red shifted absorption maximum and larger extinction coefficient resulting in better solar conversion efficiency ϕ_{sol} (Ref. 9).

Although, as it was expected, the repeated dip-coating increases the roughness factor (R_f) and the solar efficiency ϕ_{sol} , this tendency is observable only for electrodes containing less than 5 layers. For thicker films both parameters attain almost constant values despite different number of layers. Apparently, this seems to be simply a result of the almost identical roughness factor for thicker films, but there is, actually, no exact proportionality

between R_f and ϕ_{sol} . For instance, the ϕ_{sol} of a 5L film remains unaffected, if a post-deposition heat treatment at 425 to 500 °C is applied during the film fabrication (Table II.3.2.1). However, such heat treatment causes considerable drop of R_f already at the mildest conditions used (2 hours at 425°C; Table II.3.2.1). Also for the 1L film, there is no dramatic decrease in ϕ_{sol} , even if the film is treated at extreme temperatures (the maximum applicable temperature is limited by the heat stability of FTO glass).

Table II.3.2.1: The results of solar cell tests on mesoporous TiO₂ thin films prepared by repeated dip-coating.

NS: nanofibrous TiO₂ sample made by electrospinning (Elmarco product, NS stands for Nanospider™)

Other symbols are explained in the text.

Number of layers, thermal treatment	Layer thickness μm	El. area cm^2	Φ_{sol} @1Sun, %	U_{OC} mV	J_{SC} mA/cm^2	f	R_f
1L		0.156	1.08	727	2.00	0.74	161
1L, 500°C 2h		0.156	1.30	767	2.25	0.75	
1L, 425°C 2h, 525°C 2.5h		0.158	1.32	798	2.22	0.74	
1L, 525°C 2.5h		0.158	1.59	788	2.72	0.75	
1L, 550°C 2h		0.156	0.92	767	1.60	0.75	
3L	0.8	0.084	3.52	765	6.13	0.75	412
3L	1.0	0.158	4.04	799	7.0	0.72	466
5L	1.3	0.084	4.52	746	8.08	0.75	429
5L	1.3	0.158	4.34	765	7.68	0.74	429
5L, 425°C 2h	1.3	0.158	4.42	783	7.56	0.75	290
5L, 425°C 2h, 500°C 2h	1.3	0.158	4.39	758	7.91	0.73	
8L	1.9	0.158	4.63	749	8.61	0.72	
10L	2.3	0.158	4.57 4.60	748 731	8.14 8.57	0.75 0.73	539
NS+doctor blading		0.22	1.51	811	2.77	0.67	
NS+3L		0.22	3.96	723	7.93	0.69	

The solar conversion efficiency of 4.63 % was found for a 1.9 μm thick mesoporous TiO₂ film consisting of 8 layers. This value compares favorably to that of traditional films of the same thickness made by sintering of non-organized anatase nanoparticles. Obviously, the optimization of such mesoporous films for dye sensitized solar cells presents interplay

between the quality of anatase crystals and surface area. The amount of “amorphous” TiO_2 in the mesoporous film can be minimized by thermal treatment. However, prolonged calcination also causes collapse of the organized mesopore morphology and the loss of the active electrode area (roughness factor)¹¹. At present, new synthetic procedures are focused at modification of the precursor, and experiments are under way in our lab to improve the thermal stability of mesoporous TiO_2 films. In addition to this, recent results of solar conversion efficiency measurements on nanofibrous anatase are attached (NS samples, Table II.3.2.1.). The fibres were prepared by means of electrospinning from the polymer solution containing a titanium dioxide precursor and were or were not combined with mesoporous TiO_2 (NS+3L). The fibrous, as-made product contains 20% of TiO_2 and 80% of the polymer, which is finally removed by calcination. The solar conversion efficiency as high as 3.96% has been achieved for NS combined for 3 layer mesoporous film just during first, still non-optimized experiments, so it is obvious that this novel hierarchical material consisting of two different TiO_2 morphologies (*viz.* nanofibres and mesoporous framework) opens a new pathway offering further improvement of the DSC performance. The solar conversion efficiency of the analogous sample consisting of NS layer covered by nanocrystalline anatase by means of doctor-blading technique⁴⁷ was examined for comparison (see Table II.3.2.1).

II.3. 3 Anatase inverse opal

Anatase inverse opal is a macroporous solid with highly ordered porous structure over a large area, which has attracted considerable interest recently^{44,44,80-83}. Its structure is a typical example of three-dimensionally ordered macroporous solids. This emerging class of so-called hierarchically structured functional materials is becoming increasingly important in connection with the development of nanomaterials, nanotechnologies and photonics.

High refractive index of the wall material together with a pore size of hundreds nanometers (comparable to the wavelengths of visible light) are responsible for its photonic crys-

tal properties. Owing to its ability to inhibit the range of wavelengths from propagation through the material over all directions, this unique structure offers many applications in sensors, optoelectronics, chromatography, and photocatalysis. Mallouk et al³⁹ reported on the enhancement of the light harvesting efficiency of the dye-sensitized solar cell (DSC or Grätzel cell) by coupling a TiO₂ photonic crystal layer to a conventional film of TiO₂ nanoparticles. By tailoring of the stop band position, this assembly could improve the photocurrent efficiency by 26% due to localizing of the red part of solar spectrum in the composite structure³⁹.

The efficiency of the photoanode of the dye-sensitized solar cell could be strongly influenced either by structural parameters or by electrochemical properties of the composite materials of this electrode. Hence, deeper insight into the structure of anatase inverse opal together with the study of its electrochemical properties provide necessary feedback for tuning the synthetic protocol of anatase inverse opal with respect to the best performance of this structure in the dye-sensitized solar cell.

Figures II.3.3.1 a), b) confirm the regular arrangement of macropores in the powder form of inverse opal made by filling of the voids in the latex template from a propanolic solution of Ti(IV) isopropoxide. The diameter of pores is ca. 350 nm, which is smaller by ca. 30 % compared to diameters of the starting latex spheres (500 nm). The surface area S_{BET} of 40 m²/g, determined from adsorption measurements, represents the value typical for macroporous solids.

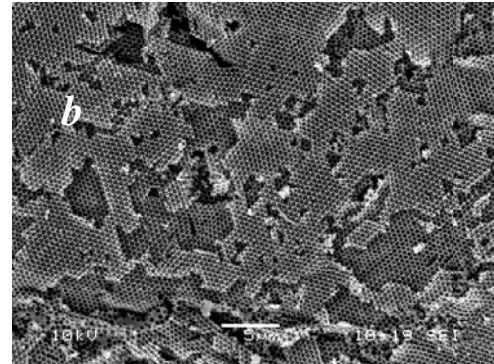
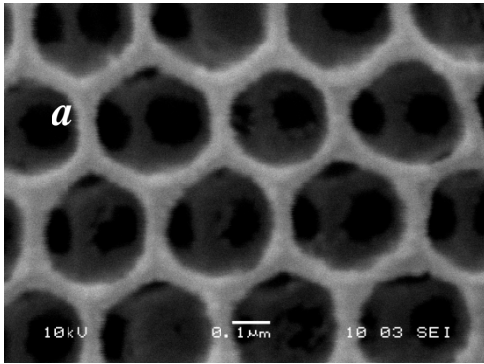


Figure II.3.3.1 a), b).

SEM pictures of the inverse opal powder made from a propanolic solution of titanium(IV) isopropoxide, scale bars correspond to 0.1 and 5 μm , respectively.

The TEM image of inverse opal in figure II.3.3.2 reveals its framework consisting of anatase nanocrystals of ca. 10-20 nm in size. X-ray diffractogram of the powder inverse opal (data not shown) can be indexed as a pure anatase phase. The crystallite size (coherent length of the crystal lattice) was approximated from the X-ray line width to be about 20 nm, which is in remarkable accord with the TEM image. The phase analysis of thin layers of inverse opal was carried out by Raman spectroscopy (data not shown). Electrochemical tests also proved the presence of phase pure anatase in the walls of our material. In contrast to SEM image of thin films prepared by liquid phase deposition indicating no ordering on the surface (data not shown), figure II.3.3.3 evidences the regular arrangement of macropores in the thin layer made by electrodeposition. In the case of liquid phase deposited layers, the inverse opal structure is covered with the compact layer of TiO_2 growing outside the voids due to the excess of the liquid precursor⁸⁴.

The position of the stop band in absorption spectra of the inverse opal structure is controlled by the diameter of latex spheres used as a template. A spectral position of the stop band for an inverse opal photonic crystal can be calculated by a modified version of Bragg's law combined with Snell's law⁸⁰:

$$(II.3.3.1)$$

where λ is the free-space wavelength of light of the stop band maximum, m is the order of Bragg diffraction, n_{avg} is the average refractive index of the macroporous material:

$$n_{avg} = [(1 - f)n_{TiO_2}^2 + fn_{air}^2]^{1/2} \quad (\text{II.3.3.2})$$

which gives $n_{avg} \cong 1.5$ for anatase inverse opal, f is the fraction of volume filling, i.e. 0.74 assuming close packing of spheres, n_{TiO_2} and n_{air} are refractive indices of TiO_2 and air, respectively, θ is the angle measured from the normal to the planes, and d_{hkl} is the interplanar spacing. For normal incidence of light ($\theta = 0^\circ$) eq. II.3.3.1 simplifies as follows⁸⁰:

$$\lambda = 2d_{hkl}n_{avg}/m \quad (\text{II.3.3.3})$$

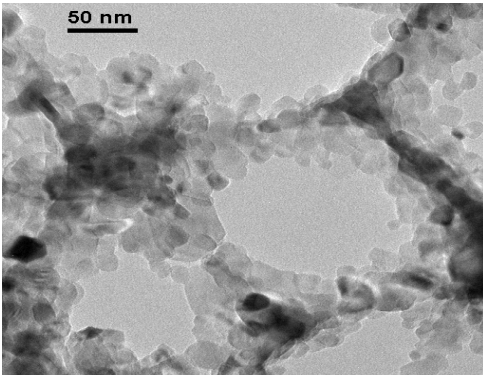


Figure II.3.3.2

TEM image of the powder form of anatase inverse opal.

By comparison of the theoretical wavelength of the stop band maximum, calculated according to eq. II.3.3.3 for the thin film of anatase inverse opal made by electrodeposition with the position of the stop band in its absorption spectrum (Figure II.3.3.4) we can either decide between the fcc or hcp ordering of air voids or evaluate the regularity of ordering over a large area. Since the interplanar spacing is different for fcc and hcp ordering of spheres of the same diameter, comparing both theoretical wavelengths calculated by means of modified version of Bragg's law with the experimental value enables to determine the factual arrangement of macropores.

Equation II.3.3.3 gives theoretical wavelength of the stop band maximum of 440 nm for the sphere diameter of 180 nm (figure II.3.3.3) and fcc ordering, which is in good agreement with the position of the stop band in the spectrum at 420-480 nm, in contrast to the value of 350 nm, calculated for hcp arrangement of the macropores.

Figures II.3.3.5 A), B) show cyclic voltammograms of Li insertion into anatase inverse opal thin film made by electrodeposition and the non-templated blank layer made by the identical procedure. The integral anodic voltammetric charge for Li-extraction of the electrode in fig. II.3.5 B) was 103 mC/cm^2 at 0.1 mV/s , which is considerably more than the corresponding value of 70 mC/cm^2 calculated for the templated electrode [Fig. II.3.3.5 A)]. The analogous trend was also observed for the integral anodic voltammetric charge determined from cyclic voltammograms of either templated or non-templated thin layers prepared by the other synthetic procedures (liquid phase deposition, vapor phase deposition; data not shown).

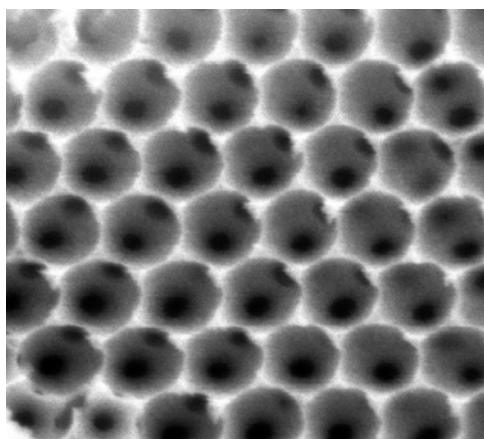


Figure II.3.3.3

SEM picture of the inverse opal layer made by electrodeposition from TiCl_3 solution, picture size $1073 \times 1073 \text{ nm}^2$.

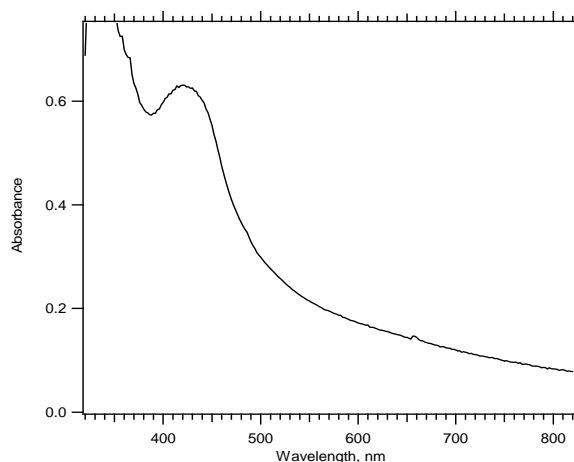


Figure II.3.3.4

UV-Vis spectrum of the anatase inverse opal thin film made from ordered latex particles of 243 nm in diameter, deposited on conducting glass.

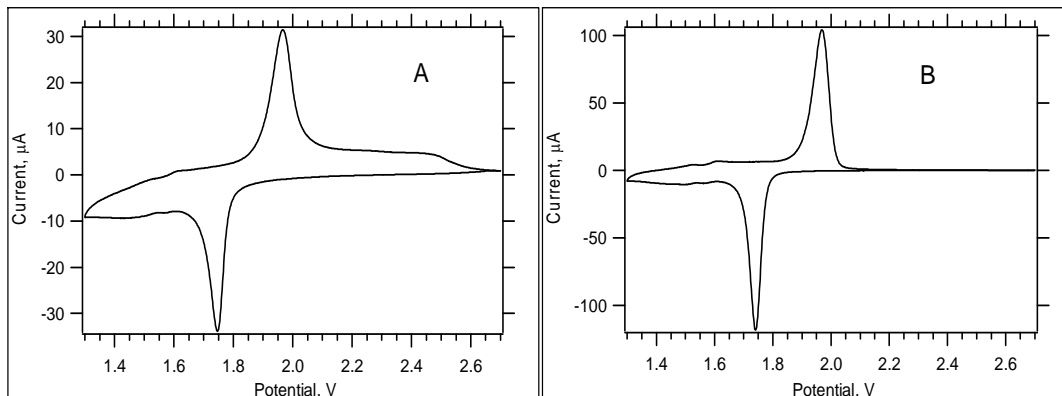


Figure II.3.3.5

Cyclic voltammograms of Li-insertion into the prepared materials. Electrolyte solution: 1 M $\text{LiN}(\text{CF}_3\text{SO}_2)_2$ + EC/DME (1:1 by volume); scan rate 0.1 mV/s. [A] Thin layer of anatase inverse opal made by electrodeposition from TiCl_3 ($10 \mu\text{A}/\text{cm}^2$, 10 hours, pH 2.4), [B] the same as [A] but non-templated

The anatase inverse opal exhibits sluggish electrochemical performance for Li-insertion as compared to that of non-templated anatase, which is probably caused by limited number of necking points resulting into poor electrical contacts between the particles in the extremely open nanocrystalline network.

II.3.4. Nanostructured $\text{TiO}_2(\text{B})$

$\text{TiO}_2(\text{B})$ accommodates Li^+ to form $\text{Li}_x\text{TiO}_2(\text{B})$. The insertion coefficient x was found 0.75-0.85 by the reaction with n-butyl-lithium, and 0.5-0.75 by electrochemistry⁸⁵⁻⁹¹. The electrochemical reversibility of lithium insertion was not very good. Recently, high electrochemical capacity ($x = 0.82$, i.e. 275 mAh/g) was reported for hydrothermally grown $\text{TiO}_2(\text{B})$ nanowires⁸⁶. The $\text{TiO}_2(\text{B})$ lattice has parallel infinite channels, in which Li^+ can be accommodated, without any significant distortion of the structure²². By the examination of phase composition of other TiO_2 materials prepared by different synthetic protocol the presence of $\text{TiO}_2(\text{B})$ was detected either in the product of hydrothermal treatment of TiO_2 in NaOH solution^{87,88} or in mesoporous titania thin films⁴⁹ prepared by supramolecular templating. Because of the presence of considerable amount of anatase in addition to $\text{TiO}_2(\text{B})$, all these materials are not appropriate for the detailed study of the electro-

chemical and photochemical behavior of $\text{TiO}_2(\text{B})$. To fulfill this task, we faced up to the challenge to develop a reliable and reproducible synthesis of phase pure $\text{TiO}_2(\text{B})$.

Nanostructured phase-pure $\text{TiO}_2(\text{B})$ with microfibrinous morphology was synthesized by newly developed protocol employing stoichiometric mixture of amorphous TiO_2 and Cs_2CO_3 as raw materials⁷ (*see* II.1.4., sample A). The diffractogram of this sample in Fig. II.3.4.1 matches well the pattern PDF No.35-0088 from JCPD, assigned to monoclinic $\text{TiO}_2(\text{B})$. Compared to $\text{TiO}_2(\text{B})$ obtained via traditional syntheses¹⁶ from $\text{K}_2\text{Ti}_4\text{O}_9$ (*see* II.1.4., sample B), the new product exhibited better electrochemical performance and stability. The diffractogram of the product B prepared by the traditional synthetic protocol¹⁶ of $\text{TiO}_2(\text{B})$ (Fig. II.3.4.1) exhibits an extra peak at $2\theta = 11.8^\circ$, which indicates some amount of unconverted hydrogen titanates, such as tetratitanate ($\text{H}_2\text{Ti}_4\text{O}_9 \cdot 0.25 \text{H}_2\text{O}$) or octatitanate ($\text{H}_2\text{Ti}_8\text{O}_{17} \cdot 0.4\text{H}_2\text{O}$) in addition to $\text{TiO}_2(\text{B})$. The presence of unconverted hydrogen titanate impurities in the sample B was confirmed also by cyclic voltammetry of Li-insertion (*see below*). SEM image of sample A (Fig. II.3.4.2) proves its fibrous morphology. Sample C (*see* II.1.4., sample C, data not shown) is a mixture of anatase and $\text{TiO}_2(\text{B})$; a typical product of calcination of hydrothermally grown layered titanates (such as $\text{H}_2\text{Ti}_3\text{O}_7$)^{86,89}.

Cyclic voltammograms of Li-insertion into the sample A contain just a pair of double peaks (so-called S-peaks; S stands for “surface”, as Li insertion into $\text{TiO}_2(\text{B})$ is considered to be the surface–confined process) at formal potential of 1.52 and 1.59 V vs. Li/Li^+ , which are ascribed to the presence of $\text{TiO}_2(\text{B})$ in the material⁹⁰ (Fig. II.3.4.3). Due to the absence of any features corresponding to the Li insertion into other TiO_2 phases (*see below*, Tab. II.3.5.1.) in aforementioned voltammogram, this fact can be considered as a proof of phase purity of the sample A. Hence, cyclic voltammetry of Li-insertion can be used as a reliable and sensitive analytical method to determine the phase composition of TiO_2 materials.

The Li-storage capacity ($\text{Li}/\text{Ti} = x$) at the slowest voltammetric scan (0.1 mV/s) was 0.68 for the respective sample.

By the analysis of the dependence between the peak current of S-peaks in the sample *A* and the scan rate the current was found to scale with the first power of scan rate, which is typical for capacitive charging:

$$i = dQ/dt = CdE/dT = Cv \quad (\text{II.3.4.1})$$

Q is the voltammetric charge, *C* is capacitance and *dE/dt* the scan rate, *v*. The peak structure with small peak-to-peak splitting (ca. 50-100 mV at *v* = 0.1 mV/s) points at a surface-confined charge transfer process, which can be considered faradaic pseudocapacitance. The found Li-storage capacity (*x* ≈ 0.5-0.7) considerably exceeds the “ordinary” capacity of the TiO₂ surface assuming solely the double-layer plus the faradaic pseudocapacitance of surface states⁹¹. Consequently, this behavior is specific for the TiO₂(B), and we may suggest that its open structure with freely accessible channels²² is responsible for the fast Li-charging of a TiO₂(B) crystal. In contrary to this, Li-insertion into anatase is diffusion controlled irreversible process^{58,59} with the peak current scaling with the square root of the scan rate (Eq. II.3.1.3.).

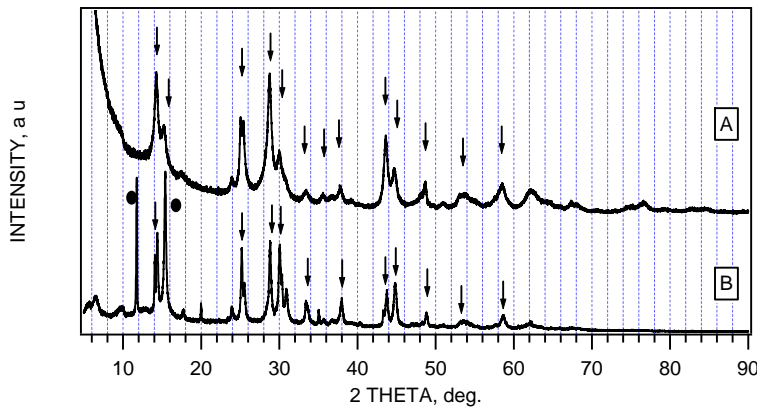


Figure II.3.4.1:

Comparison of X-ray diffractograms of sample prepared by our protocol (A) with that synthesized according to Ref. 16 (B). The plots are offset for clarity. The peaks assigned to the TiO₂(B) phase are marked by arrows, two peaks marked by full points evidence the presence of unconverted protonic titanates in the sample B.

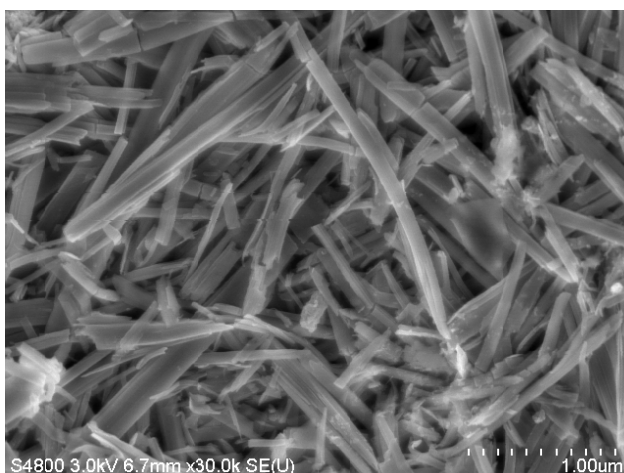


Figure II.3.4.2:

Scanning electron microscopy image of sample A. Scale bar corresponds to 1 μm.

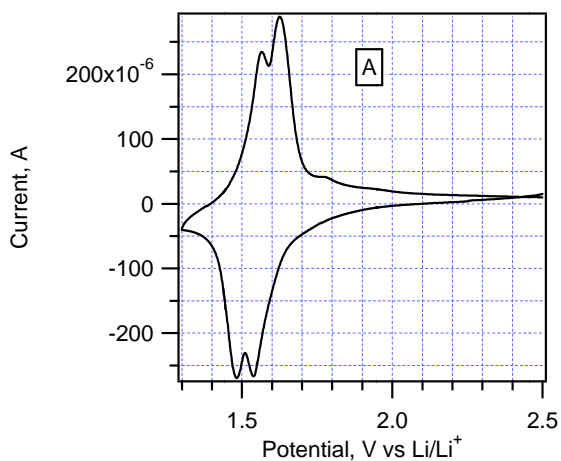


Figure II.3.4.3:

Cyclic voltammogram of sample A in 1M LiN(CF₃SO₂)₂ + EC/DME (1/1, v/v); scan rate 0.1 mV/s.

The fact that Li is accommodated in TiO₂(B) via pseudocapacitive process recalls the idea of fast transport of Li⁺ in parallel channels of the TiO₂(B) lattice²². The channels run perpendicular to (010) face of TiO₂(B) (Fig. II.3.4.4). This face is abundant at the cross-section of typical microfibrous particles of TiO₂(B).

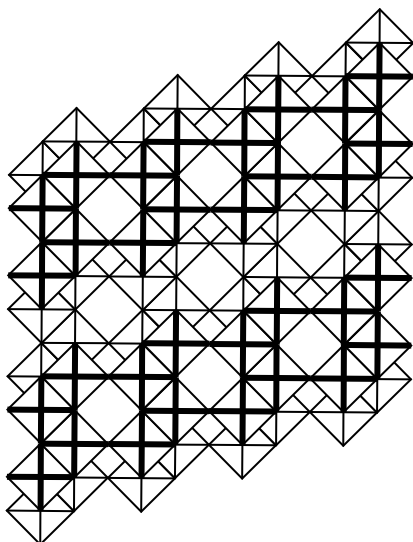


Figure II.3.4.4:

Projection of the idealized structure of $\text{TiO}_2(\text{B})$ perpendicular to the (010) face.

During electrochemical insertion, Li^+ ions interact with the whole surface of a fibrous particle. Hence, Li^+ ions, perhaps, penetrate into the bulk fiber also in radial direction, and not only through the cross-section of a fiber (channel). Assuming the channels conduct rapidly Li^+ ions inside a particle, the rate-determining process is the primary interfacial Li^+ -transfer at the fiber surface. This would provide rationale for the surface-confined, pseudocapacitive process, controlling the overall kinetics. Such a “macroscopic” model highlights the role of fiber surface. The latter is dominated by the (100) and (001) faces, but the (010) face is negligibly engaged in the Li^+ -transfer, occurring just at the tip of a fiber. We may further speculate that the two S-peaks reflect different energy barrier for Li^+ transfer at the (100) and (001) faces, which is quite reminiscent of the Li-insertion anisotropy in anatase single crystal electrode⁹².

In contrary to the photocatalytic activity of anatase having been studied since long ago for model pollutants either in gas or liquid phase, the analogous papers on $\text{TiO}_2(\text{B})$ are rare. Hence, it was challenging to examine nanocrystalline monoclinic titania as a photocatalyst for gaseous model pollutants. To the best of our knowledge there has not been carried out such a study on the photocatalytic activity of $\text{TiO}_2(\text{B})$ for gaseous reactants so far. The photocatalytic activity of $\text{TiO}_2(\text{B})$ in a gas phase was evaluated by the total oxi-

duction of propane with oxygen and the photocatalytic reduction of NO to N₂ in an oxygen rich gas mixture⁴. Using the steady state material balance equation, the reaction rate per surface area r_A of a given reaction was calculated for a given flow rate \dot{V} with the help of the concentration values of the reaction components in the incoming (c_i^0) and the effluent (c_i) flow according to the equation (II.3.4.3):

$$r_A = \frac{\dot{V}}{A} (c_i^0 - c_i) \quad (\text{II.3.4.3})$$

The quantum yield, Q [%], was defined as a parameter to characterize the reaction system:

$$Q = \left(\frac{r_A}{I_p} \right) * 100 \quad (\text{II.3.4.4})$$

wherein I_p denotes the moles of photons absorbed per second and geometric surface area of the photocatalytically active plate.

For the total oxidation of propane, the reaction rates normalized per 1 m²/g of the BET surface area of the catalyst were determined to be $1.37 \cdot 10^{-10}$ mol s⁻¹ m⁻² g and $2.5 \cdot 10^{-10}$ mol s⁻¹ m⁻² g for the sample A and Hombifine N (*see* II.2.), respectively. Considering the different phase composition of both catalysts, it is interesting to note that the anatase-free monoclinic TiO₂(B) (sample A) and pure anatase (Hombifine N) exhibit comparable reaction rates per surface area. Even more interesting are the results obtained for the photocatalytic reduction of NO to N₂ in an oxygen rich gas mixture. The quantum yields of 0.46% and 5.84% were determined for our sample A and for Hombifine N, respectively. The ratio of these values (0.08) roughly equals to the ratio of their BET surface areas (0.09). However, the special feature of the sample A is its high selectivity with respect to the NO reduction. Using Hombifine N, 0.8 molecules of propane are needed to reduce one molecule NO to 0.5 N₂, while if monoclinic TiO₂(B) is employed, only 0.4 molecules of propane are sufficient to reduce one molecule of NO.

II.3.5. Nanocrystalline spinel $\text{Li}_4\text{Ti}_5\text{O}_{12}$

The classical method of the preparation of spinel $\text{Li}_4\text{Ti}_5\text{O}_{12}$ is a solid-state reaction of stoichiometric amounts of TiO_2 and Li_2CO_3 or LiOH ; the reaction typically occurs within 12-24 h at $800\text{-}1000^\circ\text{C}$ ⁹³. This synthetic route gives microcrystalline products. Alternatively, the lithium titanate spinels can be also prepared by a reaction of butyllithium with TiO_2 or titanium(IV) isopropoxide followed by calcination above 800°C ^{94,95}. Sol-gel synthesis of $\text{Li}_4\text{Ti}_5\text{O}_{12}$ from titanium(IV) isopropoxide and lithium acetate was described by Bach et al^{96,97}. Also in this case, the calcination at 800°C was necessary to obtain a pure spinel phase. The high temperature solid-state reaction⁹³ is usually selected for the synthesis of $\text{Li}_4\text{Ti}_5\text{O}_{12}$, whereas the "butyllithium route" is preferable for the synthesis of LiTi_2O_4 ^{96,97}.

As for mesoscopic TiO_2 (anatase), the Li-insertion activity of spinel $\text{Li}_4\text{Ti}_5\text{O}_{12}$ depends markedly on the particle size and morphology. Nanocrystalline $\text{Li}_4\text{Ti}_5\text{O}_{12}$ was reported to be prepared by high energy ball milling of the conventional microcrystalline spinel⁹⁸. The product had particles around 600 nm in size, but its electrochemical performance was not significantly different from that of the non-milled starting material. Amatucci et al⁹⁹ reported recently on nanocrystalline $\text{Li}_4\text{Ti}_5\text{O}_{12}$ exhibiting a very promising charging rate and stability in a hybrid cell with a supercapacitor-like counter electrode. The nanostructured $\text{Li}_4\text{Ti}_5\text{O}_{12}$ was prepared by high-temperature reaction of TiO_2 and Li_2CO_3 .

The "truly" nanosized oxide materials (1-5 nm particles) exhibiting qualitatively different Li-insertion electrochemistry was prepared by an alternative synthetic protocol employing the hydrolysis of parent alkoxides (sol-gel)⁹³. The average particles size, d_p was estimated by assuming nonporous spherical grains of a density of $\rho = 3.5 \text{ g/cm}^3$ and the given surface area, S_{BET}

$$d_p = 6/\rho S_{\text{BET}} \quad (\text{II.3.5.1})$$

which gives $d \sim 9$ nm for $S = 183$ m²/g. This value is roughly in agreement with that determined from X-ray linewidth, w by means of Scherrer formula

$$d_c = 0.9\lambda/w\cos\theta \quad (\text{II.3.5.2})$$

where θ is the diffraction angle and λ is the CuK α X-ray wavelength (0.1540562 nm). Equation II.3.5.2 gives a d_c of about 4-5 nm. The phase analysis of the product carried out by X-ray diffraction evidenced the presence of almost pure spinel Li₄Ti₅O₁₂ with about less than 1% of anatase impurities⁹³.

Cyclic voltammogram of material evidences the presence of two peaks at formal potential of 1.56 V vs Li/Li⁺, which could be ascribed to Li insertion into Li₄Ti₅O₁₂ spinel. The small peaks at 1.75 and 2.0 V can be assigned to trace impurities of anatase⁹³. So the cyclic voltammetry of Li insertion is beneficial not just for the electrochemical performance evaluation, but also for the phase analysis, as it is further demonstrated.

Table II.3.5.1:

Li insertion properties of various Ti(IV) oxide phases: E_f stands for formal potential of Li insertion to the respective Li-Ti-O phase; x is the ratio of inserted Li⁺ per one Ti(IV) (see Eq. II.3.1.1.)

Structure	Formula	E_f, V_{Li}	x
Rutile	TiO ₂	1.47	0.3
Anatase	TiO ₂	1.85	0.5
Brookite	TiO ₂	-	"small"
Bronze	TiO ₂ (B)	1.5	0.5 – 0.9
Ramsdellite	TiO ₂	1.4 & 2.3	0.6
Ramsdellite	LiTi ₂ O ₄	1.3 & 2.2	0.6
Ramsdellite	Li ₂ Ti ₃ O ₇	1.3 & 2.2	0.5
Spinel	LiTi ₂ O ₄	1.56	0.5
Spinel	Li ₄ Ti ₅ O ₁₂	1.55	0.5
Monoclinic	Li ₂ TiO ₃	-	0

Spinel Li₄Ti₅O₁₂ synthetic protocol based on precipitation of TiO₂ from the solution of Li and Ti alkoxides in absolute ethanol⁹³ was upgraded. Slight modification of the calcination procedure avoided the presence of any anatase impurities in final product. The analysis by means of both X-ray diffraction and cyclic voltammetry of Li insertion proved

phase purity of prepared $\text{Li}_4\text{Ti}_5\text{O}_{12}$ spinel⁴. The other materials used for the study of the dependence between the particle size and charge capacity were purchased from Titan Kogyo (microcrystalline spinel LT-2) and Altair NanoMaterials⁴.

The effect of particle size on charging rate of $\text{Li}_4\text{Ti}_5\text{O}_{12}$ was evaluated by galvanostatic chronopotentiometry, while the charge/discharge current was adjusted to C2, C50, C100, C150, C200 and C250. The maximum charge is, essentially, proportional to the film's mass, and its determination is easy and precise, either from slow cyclic voltammetry (scan rates ≤ 1 mV/s) or galvanostatic chronopotentiometry at low currents ($\leq C2$). According to eq. I.2.2 the maximum charge capacity of $\text{Li}_4\text{Ti}_5\text{O}_{12}$ equals 175 mAh/g based on the mass of the starting host material. However, real electrodes tend to deliver about 150-160 mAh/g.

Galvanostatic chronopotentiometric measurements proved the differences in electrochemical performance of commercial microcrystalline (LT-2, Titan Kogyo, $3\text{m}^2/\text{g}$) and laboratory-made nanocrystalline spinel $\text{Li}_4\text{Ti}_5\text{O}_{12}$. The maximum reversible Li-insertion capacity is 175 mAh/g, and in case of nanocrystalline product about 70% of this charge can still be cycled at 250C with the same cutoff voltage. The commercial microcrystalline $\text{Li}_4\text{Ti}_5\text{O}_{12}$ shows only *ca.* 19% of its nominal capacity in the 250C charging/discharging cycle⁹³. The efficient Li insertion was observed for all thin-layer electrodes prepared by our sol-gel route; marked differences were traced between materials having different surface areas. Since this effect cannot be simply interpreted in terms of Li^+ diffusion or by poor electrical contact, the dependence between charge capability and the particle size of the spinel $\text{Li}_4\text{Ti}_5\text{O}_{12}$ was subjected to a detailed study.

Systematic screening of $\text{Li}_4\text{Ti}_5\text{O}_{12}$ materials with the particle size within a broad range shows that while the charge capabilities of microcrystalline spinel are roughly proportional to the specific surface areas, if the latter are smaller than *ca.* $20\text{ m}^2/\text{g}$. On the other hand, for materials having surface areas between *ca.* 20 to $100\text{ m}^2/\text{g}$ they attain the value almost independent of the surface area and close to the nominal capacity of the given material (referred to the value at 2C) (Fig.II.3.5.1). In other words, the accessible charging

rate does not seem to be limited by particle-sizes, if they are between ca. 80 to 20 nm (Ref.4).

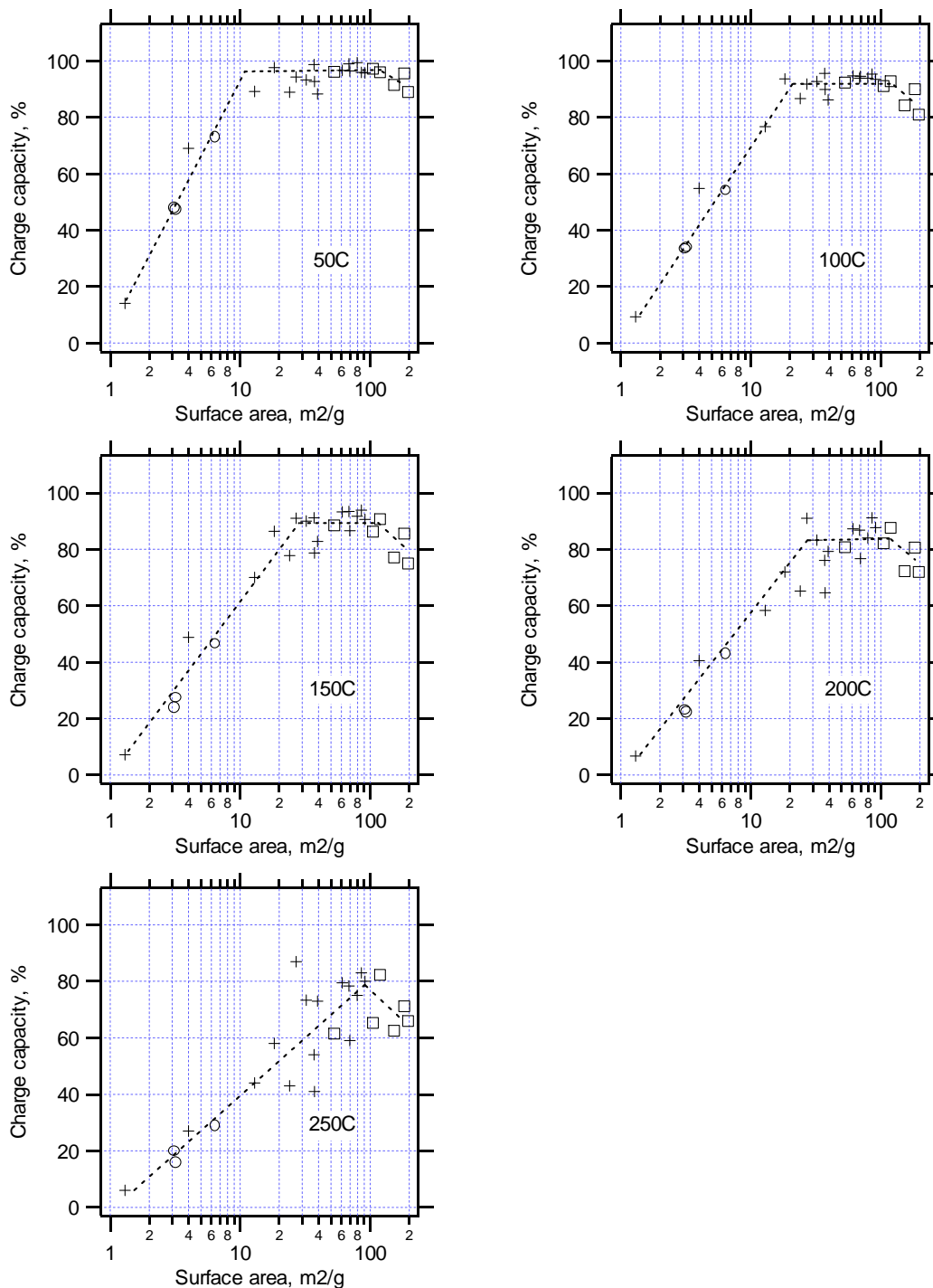


Figure II.3.5.1: Charge capacity (referred to a nominal charge capacity) of $\text{Li}_4\text{Ti}_5\text{O}_{12}$ materials with varying surface areas (Altair samples +, Titan Kogyo samples o, laboratory made alkoxide route samples \square). The charging rate was 50C, 100C, 150C and 200C, respectively for the given plots. The charge capacity was determined from galvanostatic chronopotentiometry with the cut-off voltages of 3 and 1 V. The nominal charge capacity was determined from slow cyclic voltammetry at scan rates $<1\text{mV/s}$. Electrolyte solution: 1 M $\text{LiN}(\text{CF}_3\text{SO}_2)_2$ + EC/DME (1:1, v:v).

Despite favorable particle size (below 20 nm) the high-rate charge capability is not kept for particles with surface areas $>100 \text{ m}^2/\text{g}$.

The slow response of ultrasmall particles is probably not caused by poor electrical contacts. The excellent charging rate of nanocrystalline $\text{Li}_4\text{Ti}_5\text{O}_{12}$ is clearly demonstrated especially in the optimized range of particles sizes, i.e. 20-80 nm(Ref.4). However, small particles tend to show larger charge irreversibility at low currents and deep cathodic cut-off potentials. This may be due to an enhanced possibility of adsorption of reducible impurities (such as humidity) on the large-area materials or impurities in the lattice or poorly formed lattice due to low temperature processing of some of the samples. Big particles are less sensitive to parasitic reactions, such as irreversible reduction of adsorbed protons. Our analysis points at spinel particles between 20-80 nm as the optimum robust size, taking in to consideration manufacturing, handling, and providing high charging rates with good reversibility.

If we assume that the current after a potential step, I is controlled by diffusion, the chronoamperometric plot should formally obey the Cottrell equation:

$$I = S_{el}FD^{1/2}c\pi^{1/2}t^{-1/2} \quad (\text{II.3.5.3})$$

S_{el} is the "true" (physical) electrode area, c is concentration of Li^+ in the solid and D is chemical diffusion coefficient. This formalism is valid for Li^+ insertion into anatase, both single crystal and nanocrystalline electrodes^{47,49}. To calculate the diffusion coefficients of our spinels, the physical electrode area, S_{el} , was approximated by its BET area. The film's mass was re-calculated from the maximum reversible charge assuming the nominal specific charge capacity of 175 mAh/g of a fresh electrode (cf. Eq. I.2.2).

Concentration c is equivalent to three extra Li^+ ions in the $\text{Li}_4\text{Ti}_5\text{O}_{12}$ molecule, which translates into $c = 21.9 \text{ mmol}/\text{cm}^3$. This concentration of Li^+ occurs in a thin layer underneath the surface, shortly after the cathodic potential step. Immediately after the application of the subsequent anodic step, the same Li^+ concentration occurs in the bulk, but a

thin layer underneath the surface has $c \rightarrow 0$. This is the driving force for Li^+ transport, if we neglect migration of Li^+ in the electrical field.

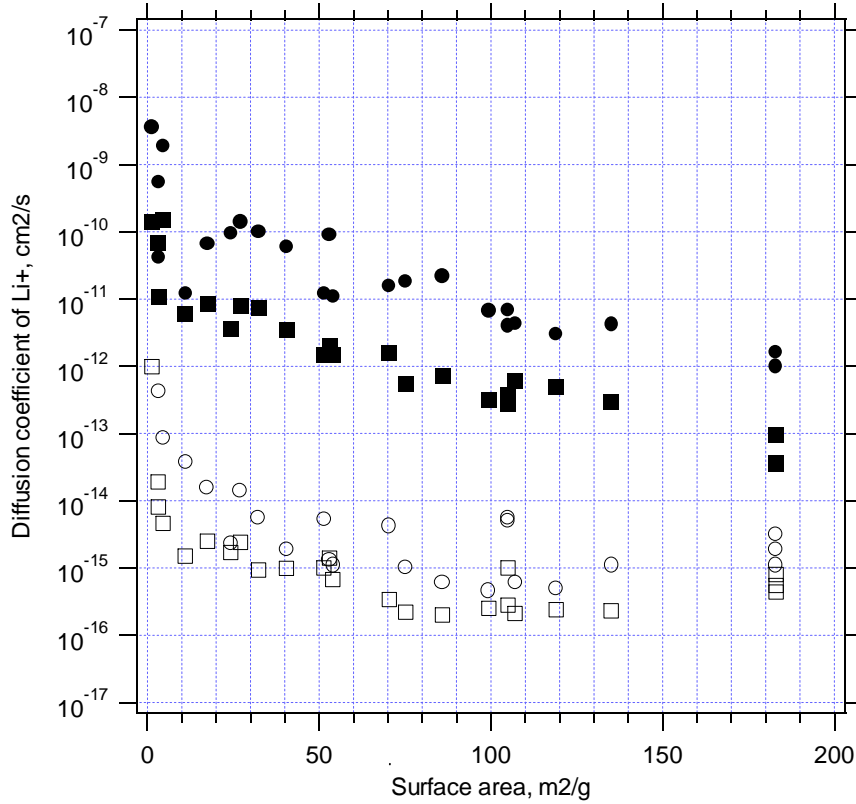


Figure II.3.5.2:

Solid-state diffusion coefficients of Li^+ in the $\text{Li}_4\text{Ti}_5\text{O}_{12}$ electrodes determined from chronoamperometric measurements. (●) long-time anodic step (○) short-time anodic step (■) long-time cathodic step (□) short-time cathodic step⁴.

The D values, shown in Fig. II.3.5.2, are smaller than those, found for $\text{Li}_4\text{Ti}_5\text{O}_{12}$ by using neutron radiography¹⁰⁰ (10^{-6} cm^2/s) or cyclic voltammetry⁹⁸ ($2 \cdot 10^{-8}$ cm^2/s). The values of D illustrate that the micron-sized crystals can hardly be charged with Li^+ efficiently at rates around 200 C. The effective diffusion distance, δ equals:

$$\delta = (\pi Dt)^{1/2} \quad (\text{II.3.5.4})$$

where the time $t = 18$ s, if we assume the charging rate 200C. Assuming $D \approx 10^{-12}$ cm^2/s (for Li-insertion into coarse particles), the diffusion distance is only $\delta \approx 75$ nm from Eq.

II.3.5.4. Hence, the micron-sized crystal cannot be filled with Li^+ completely at the 200C charging. This seems to point clearly at nanocrystalline materials as better host structures for fast Li^+ charging. However, the situation is more complex, since the diffusion coefficients are also smaller in nanocrystalline materials. The optimum material has to be chosen as a compromise between the rate of Li^+ transport and the crystal size.

III. CONCLUSIONS

It has been known for a long time that material properties change on the nanoscale and are different from those of single crystals or conventional microstructured, monolithic or composite materials³². The presented thesis aimed at demonstration of the diversity in these properties for various morphologies of TiO_2 . Despite the fact that the chemical composition is identical, the structure of different morphologies matters and it is responsible for their specialty. The successfully mastered syntheses of desirable particle size materials open the pathway towards applications taking advantage of size dependent properties. DSC employing $2\mu\text{m}$ mesoporous TiO_2 film as a photoanode exhibited the solar conversion efficiency as high as 4.63% due to the large surface area (roughness factor). Optimized pore size together with the framework consisting of anatase nanocrystals are responsible for the high dye adsorption capacity improving the performance.

Incorporating an additional inverse opal layer in DSC represents an example of its further possible upgrade. This optimized set up can increase the short circuit photocurrent efficiency of this device of about 26 % (Ref.39).

Owing to the diffusion coefficient of an order of $10^{-13} \text{ cm}^2/\text{s}$ for microcrystalline spinel and even less for nanocrystalline spinel particles, the particle size represents an important factor for battery applications. While Li^+ diffusion into material of 100 nm in diameter takes about 2000 s, 10 nm particle can be fully charged in 20 s. Despite the drop of the solid-state Li^+ -diffusion coefficients by orders of magnitude for nanocrystalline particles, obviously due to the larger stress induced by the Li^+ - Li^+ repulsion, the charging of nanocrystalline particles is still much faster as compared to microcrystalline ones. The slow

Li^+ -transport in small particles is not rate limiting, because the insertion occurs only in short distances underneath the surface and in overall performance it is fully compensated by the increase of the active electrode area.

Synthetic protocol leading to the preparation of phase pure nanocrystalline $\text{TiO}_2(\text{B})$ enables to produce this material in sufficient quantity and quality for possible applications based on the unique electrochemical behavior of this titanium dioxide polymorph. The $\text{TiO}_2(\text{B})$ host accommodates lithium by a pseudocapacitive faradaic process, which is not controlled by diffusion.

To improve further an electrochemical performance of this material, composites of TiO_2 nanocrystals with single walled carbon nanotubes (SWNT) were prepared and their behavior was studied recently^{101,102}. The nanocrystals deposited on SWNT by electrochemical deposition correspond to anatase phase with small amount of monoclinic $\text{TiO}_2(\text{B})$. While explored by cyclic voltammetry of Li^+ insertion, the Li^+ insertion coefficient, x of 0.42 was found¹⁰¹.

In general, the particle size and morphology of titanium dioxide materials seems to be almost of the same importance as their phase composition, as far as chemical and electrochemical properties, and applicability is concerned. Tailoring of the synthetic procedure towards products with desirable morphology is the right way to obtain materials with desirable properties and, subsequently, of a great application potential.

Reference List

- (1) Attia, A.; Zukalova, M.; Rathousky, J.; Zukal, A.; Kavan, L. *J. Solid State Electrochem.* **2005**, *9*, 138.
- (2) Attia, A.; Zukalova, M.; Pospisil, L.; Kavan, L. *J. Solid State Electrochem.* **2007**, *11*, 1163.
- (3) Kalbac, M.; Zukalova, M.; Kavan, L. *J. Solid State Electrochem.* **2003**, *8*, 2.
- (4) Kavan, L.; Prochazka, J.; Spitler, T.M.; Kalbac, M.; Zukalova, M.; Drezen, T.; Grätzel, M. *J. Electrochem. Soc.* **2003**, *150*, A1000-A1007
- (5) Kavan, L.; Kalbac, M.; Zukalova, M.; Exnar, I.; Lorenzen, V.; Nesper, R.; Grätzel, M. *Chem. Mater.* **2004**, *16*, 477.
- (6) Kavan, L.; Zukalova, M.; Kalbac, M.; Grätzel, M. *J. Electrochem. Soc.* **2004**, *151*, A1301-A1307
- (7) Zukalova, M.; Kalbac, M.; Kavan, L.; Exnar, I.; Grätzel, M. *Chem. Mater.* **2005**, *17*, 1248.
- (8) Zukalova, M.; Kalbac, M.; Kavan, L.; Exnar, I.; Haeger, A.; Grätzel, M. *Prog. Solid St. Chem.* **2005**, *33*, 253.
- (9) Zukalova, M.; Zukal, A.; Kavan, L.; Nazeeruddin, M.K.; Liska, P.; Grätzel, M. *Nano Lett.* **2005**, *5*, 1789.
- (10) Zukalova, M.; Kalbac, M.; Kavan, L. In *Nanoengineered Assemblies and Advanced Micro/Nanosystems Proceedings*; Taylor, D.P., Liu, J., McIlroy, D., Merhari, L., Pendry, J.B., Borenstein, J.T., Eds.; MRS: Warrendale, 2004; pp R531-R536
- (11) Zukalova, M.; Prochazka, J.; Zukal, A.; Yum, J.H.; Kavan, L. *Inorg. Chim. Acta* **2008**, *361*, 656.
- (12) Prochazka, J.; Kavan, L.; Shklover, V.; Zukalova, M.; Frank, O.; Kalbac, M.; Zukal, A.; Pelouchova, H.; Janda, P.; Mocek, K.; Klementova, M.; Carbone, D. *Chem. Mater.* **2008**, *accepted*,
- (13) van de Krol, R. Lithium Intercalation in Anatase TiO₂. 2000.
- (14) Swamy, V.; Gale, J.D.; Dubrovinsky, L.S. *J. Phys. Chem. Solids* **2001**, *62*, 887.
- (15) Banfield, J.; Veblen, D.; Smith, D. *Amer. Mineralogist* **1991**, *76*, 343.
- (16) Marchand, R.; Brohan, L.; Tournoux, M. *Mat. Res. Bull.* **1980**, *15*, 1129.

- (17) Latroche, M.; Brohan, L.; Marchand, R.; Tournoux, M. *J. Solid State Chem.* **1989**, *81*, 78.
- (18) Akimoto, J.; Gotoh, Y.; Oosawa, Y.; Nonose, N.; Kumagai, T.; Aoki, K.; Takei, H. *J. Solid State Chem.* **1994**, *113*, 27.
- (19) Dubrovinsky, L.S.; Dubrovinskaia, N.A.; Swamy, V.; Muscat, J.; Harrison, N.M.; Ahuja, R.; Holm, B.; Johansson, B. *Nature* **2001**, *410*, 653.
- (20) Sato, H.; Endo, S.; Sugiyama, M.; Kukegawa, T.; Shimomura, O.; Kusaba, K. *Science* **1991**, *251*, 786.
- (21) Tang, J.; Endo, S. *J. Amer. Ceram. Soc.* **1993**, *76*, 796.
- (22) Nuspl, G.; Yoshizawa, K.; Yamabe, T. *J. Mater. Chem.* **1997**, *7*, 2529.
- (23) Yin, S.; Wu, J.; Aki, M.; Sato, T. *Int. J. Inorg. Mat.* **2000**, *2*, 325.
- (24) Yin, S.; Fujishiro, Y.; Wu, J.; Aki, M.; Sato, T. *J. Mater. Proc. Technol.* **2003**, *137*, 45.
- (25) Bakardjieva, S.; Subrt, J.; Stengl, V.; Dianez, M.J.; Sayagues, M.J. *Applied Catalysis B-Environmental* **2005**, *58*, 193.
- (26) Bakardjieva, S.; Subrt, J.; Stengl, W.; Vecernikova, E.; Bezdiccka, P. *Solid State Chemistry V* **2003**, *90-91*, 7.
- (27) Betz, G.; Tributsch, H.; Marchand, R. *J. Appl. Electrochem.* **1984**, *14*, 315.
- (28) Deschanvers, A.; Raveau, B.; Sekkal, Z. *Mat. Res. Bull.* **1971**, *6*, 699.
- (29) Colbow, K.M.; Dahn, J.R.; Haering, R.R. *J. Power Sources* **1989**, *26*, 397.
- (30) Ohzuku, T.; Ueda, A.; Yamamoto, N. *J. Electrochem. Soc.* **1995**, *142*, 1431.
- (31) Ferg, E.; Gummov, R.J.; de Kock, A.; Thackeray, M.M. *J. Electrochem. Soc.* **1994**, *141*, L147-L150
- (32) Gogotsi, Y. *Nanomaterials Handbook*; 2006;
- (33) Zhang, H.; Banfield, J.F. *J. Phys. Chem. B* **2000**, *104*, 3481.
- (34) Jamnik, J.; Maier, J. *Phys. Chem. Chem. Phys.* **2003**, *5*, 5215.
- (35) Levi, M.D.; Aurbach, D. *Electrochim. Acta* **1999**, *45*, 167.
- (36) Choi, Y.M.; Pyun, S.I. *Solid State Ionics* **1997**, *99*, 173.
- (37) Chen, X.; Mao, S.S. *J. Nanosci. Nanomat.* **2006**, *6*, 906.

- (38) Kavan, L.; O'Regan, B.; Kay, A.; Grätzel, M. *J. Electroanal. Chem.* **1993**, *346*, 291.
- (39) Nishimura, S.; Abrams, N.; Lewis, B.A.; Halaoui, L.I.; Mallouk, T.E.; Benkstein, K.D.; Van de Langemaat, J.; Frank, A.J. *J. Am. Chem. Soc.* **2003**, *125*, 6306.
- (40) Nishimura, S.; Shishido, A.; Abrams, N.; Mallouk, T.E. *Appl. Phys. Lett.* **2002**, *81*, 4532.
- (41) Kishimoto, H.; Takahama, K.; Hashimoto, N.; Aoi, Y.; Deki, S. *J. Mater. Chem.* **1998**, *8*, 2019.
- (42) Miyasaka, T.; Kijitori, Y.; Muramaki, T.N.; Kimura, M.; Uegusa, S. *Chem. Lett.* **2002**, 1250.
- (43) Wijnhoven, J.E.G.J.; Vos, W.L. *Science* **1998**, *281*, 302.
- (44) Holland, B.T.; Blanford, C.F.; Stein, A. *Science* **1998**, *281*, 538.
- (45) Zhang, H.; Finnegan, M.; Banfield, J.F. *Nano Letters* **2001**, *1*, 81.
- (46) Nazeeruddin, M.K.; Kay, A.; Rodicio, I.; Humphry-Baker, R.; Mueller, E.; Liska, P.; Vlachopolous, N.; Grätzel, M. *J. Am. Chem. Soc.* **1993**, *115*, 6382.
- (47) Kavan, L.; Grätzel, M.; Rathousky, J.; Zukal, A. *J. Electrochem. Soc.* **1996**, *143*, 394.
- (48) Kavan, L.; Attia, A.; Lenzmann, F.; Elder, S.H.; Grätzel, M. *J. Electrochem. Soc.* **2000**, *147*, 2897.
- (49) Kavan, L.; Rathousky, J.; Grätzel, M.; Shklover, V.; Zukal, A. *J. Phys. Chem. B* **2000**, *104*, 12012.
- (50) Elder, S.H.; Gao, X.; Li, J.; Liu, D.; McCready, D.E.; Windisch, C.F. *Chem. Mater.* **1998**, *10*, 3140.
- (51) Kavan, L.; Grätzel, M.; Gilbert, S.E.; Klemenz, C.; Scheel, H.J. *J. Am. Chem. Soc.* **1996**, *118*, 6716.
- (52) Li, F.; Zhang, L.; Metzger, R.M. *Chem. Mater.* **1998**, *10*, 2470.
- (53) Lin, Y.; Wu, G.S.; Yuan, X.Y.; Xie, T.; Zhang, L.D. *J. Phys. Condens. Matter* **2003**, *15*, 2917.
- (54) Matsumoto, Y.; Ishikawa, Y.; Nishida, M.; Seiichiro, I. *J. Phys. Chem. B* **2000**, *104*, 4204.
- (55) Michailowski, A.; AlMawlawi, D.; Cheng, G.; Moskovits, M. *Chem. Phys. Lett.* **2001**, *349*, 1.

- (56) Zhang, X.; Yao, B.; Zhao, L.; Llang, C.; Zhang, L.; Mao, Y. *J. Electrochem. Soc.* **2001**, *148*, G398-G400
- (57) Zhang, H.; Banfield, J.F. *J. Mater. Res.* **2000**, *15*, 437.
- (58) Lindström, H.; Södergen, S.; Solbrand, A.; Rensmo, H.; Hjelm, J.; Hagfeldt, A.; Lindquist, S.E. *J. Phys. Chem. B* **1997**, *101*, 7717.
- (59) Van de Krol, R.; Goossens, A.; Schoonman, J. *J. Phys. Chem. B* **1999**, *103*, 7151.
- (60) Lindström, H.; Södergen, S.; Solbrand, A.; Rensmo, H.; Hjelm, J.; Hagfeldt, A.; Lindquist, S.E. *J. Phys. Chem. B* **1997**, *101*, 7710.
- (61) Bartl, M.H.; Boettcher, S.W.; Frindell, K.L.; Stucky, G.D. *Acc. Chem. Res.* **2005**, *38*, 263.
- (62) Putnam, R.L.; Nakagawa, N.; McGrath, K.M.; Yao, N.; Aksay, I.A.; Gruner, S.M.; Navrotsky, A. *Chem. Mater.* **1997**, *9*, 2690.
- (63) Takahashi, R.; Takenaka, S.; Sato, S.; Sodesawa, T.; Ogura, K.; Nakanishi, K. *J. Chem. Soc. Faraday Trans.* **1998**, *94*, 3161.
- (64) Yang, P.; Zhao, D.; Margolese, D.I.; Chmelka, B.F.; Stucky, G.D. *Nature* **1998**, *396*, 152.
- (65) Yang, P.; Zhao, D.; Margolese, D.I.; Chmelka, B.F.; Stucky, G.D. *Chem. Mater.* **1999**, *11*, 2813.
- (66) Alberius, P.C.A.; Frindell, K.L.; Hayward, R.C.; Kramer, E.J.; Stucky, G.D.; Chmelka, B.F. *Chem. Mater.* **2002**, *14*, 3284.
- (67) Crepaldi, E.L.; Soller-Illia, G.J.A.A.; Grosso, D.; Cagnol, F.; Ribot, F.; Sanchez, C. *J. Am. Chem. Soc.* **2003**, *125*, 9770.
- (68) Grosso, D.; Soller-Illia, G.J.A.A.; Babonneau, F.; Sanchez, C.; Albouy, P.A.; Brunneau, A.B.; Balkenende, A.R. *Adv. Mater.* **2001**, *13*, 1085.
- (69) Boettcher, S.W.; Bartl, M.H.; Hu, J.G.; Stucky, G.D. *J. Am. Chem. Soc.* **2005**, *127*, 9721.
- (70) Grosso, D.; Cagnol, F.; Soller-Illia, G.J.A.A.; Crepaldi, E.L.; Amenitsch, H.; Brunet-Bruneau, A.; Bourgeois, A.; Sanchez, C. *Adv. Funct. Mater.* **2004**, *14*, 309.
- (71) Coakley, K.M.; Liu, Y.; McGehee, M.D.; Frindell, K.L.; Stucky, G.D. *Adv. Funct. Mater.* **2003**, *13*, 301.
- (72) Park, N.G.; Schlichthörl, J.; Van de Lagemaat, J.; Cheong, H.M.; Mascarenhas, A.; Frank, A.J. *J. Phys. Chem. B* **1999**, *103*, 3308.

- (73) Choi, S.Y.; Mamak, M.; Coombs, N.; Chopra, N.; Ozin, G.A. *Adv. Funct. Mater.* **2004**, *14*, 335.
- (74) Bartl, M.H.; Boettcher, S.W.; Hu, E.L.; Stucky, G.D. *J. Am. Chem. Soc.* **2004**, *126*, 10826.
- (75) Coakley, K.M.; McGehee, M.D. *Appl. Phys. Lett.* **2005**, *83*, 3380.
- (76) Bartl, M.H.; Puls, S.P.; Tang, J.; Lichtenegger, H.C.; Stucky, G.D. *Angew. Chem.* **2005**, *119*, 3099.
- (77) Hou, K.; Tian, B.; Li, F.; Bian, Z.; Zhao, D.; Huang, C. *J. Mater. Chem.* **2005**, *15*, 2414.
- (78) Grätzel, M. *Nature* **2001**, *414*, 338.
- (79) Law, M.; Greene, L.E.; Johnson, J.C.; Saykaly, R.; Yang, P. *Nature Mat.* **2005**, *4*, 455.
- (80) Schroden, R.C.; Al-Daous, M.; Blanford, C.F.; Stein, A. *Chem. Mater.* **2002**, *14*, 3305.
- (81) Stein, A.; Schroden, R.C. *Current Opinion in Solid State and Material Science* **2001**, *5*, 553.
- (82) Johnson, N.P.; McComb, D.W.; Richel, A.; Treble, B.M.; De La Rue, R.M. *Synth. Metals* **2001**, *116*, 469.
- (83) Gu, Z.Z.; Kubo, S.; Fujishima, A.; Sato, O. *Appl. Phys. A* **2002**, *74*, 127.
- (84) Janda, P.; Weber, J.; Kavan, L. *J. Electroanal. Chem.* **1984**, *180*, 109.
- (85) Zachau-Christiansen, B.; West, K.; Jacobsen, T.; Skaarup, S. *Solid State Ionics* **1992**, *53-56*, 364.
- (86) Armstrong, A.R.; Armstrong, G.; Canales, J.; Bruce, P.G. *Angew. Chem. Int. Ed.* **2004**, *43*, 2286.
- (87) Kasuga, T.; Hiramatsu, M.; Hoson, A.; Sekino, T.; Niihara, K. *Langmuir* **1998**, *14*, 3160.
- (88) Nishizawa, H.; Aoki, Y. *J. Solid State Chem.* **1985**, *56*, 158.
- (89) Gao, X.; Zhu, H.; Pan, G.; Ye, S.; Lan, Y.; Wu, F.; Song, D. *J. Phys. Chem. B* **2004**, *108*, 2868.
- (90) Samec, Z.; Homolka, D.; Marecek, V.; Kavan, L. *J. Electroanal. Chem.* **1983**, *145*, 213.

- (91) Kavan, L.; Kratochvilová, K.; Grätzel, M. *J. Electroanal. Chem.* **1995**, 394, 93.
- (92) Hengerer, R.; Kavan, L.; Krtil, P.; Grätzel, M. *J. Electrochem. Soc.* **2000**, 147, 1467.
- (93) Kavan, L.; Grätzel, M. *Electrochem. Solid State Lett.* **2002**, 5, A39-A42
- (94) Pyun, S.I.; Kim, S.W.; Shin, H.C. *J. Power Sources* **1999**, 81-82, 248.
- (95) Murphy, D.W.; Greenblatt, M.; Zahurak, S.M.; Cava, R.J.; Waszczak, J.V.; Hull, G.W.; Hutton, R.S. *Revue de Chimie Minerale* **1982**, 19, 441.
- (96) Bach, S.; Pereira-Ramos, J.P.; Baffier, N. *J. Mater. Chem.* **1998**, 8, 251.
- (97) Bach, S.; Pereira-Ramos, J.P.; Baffier, N. *J. Power Sources* **1999**, 81-82, 273.
- (98) Zaghib, K.; Simoneau, M.; Armand, M.; Gauthier, M. *J. Power Sources* **1999**, 81-82, 300.
- (99) Amatucci, G.G.; Badway, F.; Du Pasquier, A.; Zheng, T. *J. Electrochem. Soc.* **2001**, 148, A930-A939
- (100) Takai, S.; Kamata, M.; Fujine, S.; Yoneda, K.; Kanda, K.; Esaka, T. *Solid State Ionics* **1999**, 123, 165.
- (101) Frank, O.; Kalbac, M.; Kavan, L.; Zukalova, M.; Prochazka, J.; Klementova, M.; Dunsch, L. *Phys. Stat. Sol. (b)* **2007**, 244, 4040.
- (102) Kalbac, M.; Frank, O.; Kavan, L.; Zukalova, M.; Prochazka, J.; Klementova, M.; Dunsch, L. *J. Electrochem. Soc.* **2007**, 154, K19-K24

Acknowledgement

First of all I would like to thank Professor Ladislav Kavan for his kind and permanent support, valuable advice and for allowing me to realize freely my own ideas in experiments. I also appreciate his patience with the completion of my thesis taking sometimes too long.

I would like to express my thanks to professor Graetzel for the opportunity to spend my short term scientific missions in his laboratory in Lausanne.

Special thanks to Arnost Zikal for his help and advice in the field of adsorption measurements and the interpretation of results.

Last but not least I am grateful to my colleagues Martin Kalbac, Otakar Frank and Jan Prochazka for their help and cooperation as well as for the relaxed atmosphere they provided at work.

Curriculum vitae of RNDr. Markéta Zukalová, born Houdková

Home address: Kaňkovského 1236, Praha 8, CZ-182 00, Phone: +420266053985
E-Mail: marketa.zukalova@jh-inst.cas.cz, born on 23. 3. 1964 in Prague, married, three children

Education:

- 9/70 - 6/82 Primary and secondary schools in Prague, Czech Republic, General certificate of Secondary Education: May 1982
- 1982 – 1987: Charles University in Prague, Faculty of Science, Department of Physical Chemistry
- 1987 Master thesis in Physical Chemistry: *Polymerization of phenylacetylene catalyzed by $WOCl_4+Ph_4Sn$ in benzene and benzene-dioxane*, supervisor: Prof. Dr. J. Vohlídal
- 1987 RNDr., Charles University in Prague
- 1991 - 1995 maternity leave
- 1998 – 2001 maternity leave
- 2002 started with PhD study at the Charles University in Prague,
Topic: *Organized Nanostructured TiO_2 Materials: Synthesis Characterization, Applications*: supervisors: Ing. Jiří Rathouský, CSc and Prof. RNDr. Ladislav Kavan, DSc
- 2004 FCE (First Certificate in English)

Work experience:

- Since 1987 employed as a researcher at the J. Heyrovsky Institute of Physical Chemistry, Academy of Sciences of the Czech Republic. Fields of research: Advanced sol-gel techniques, mesoporous molecular sieves with controlled morphological properties, synthesis and characterization of new types of TiO_2 nanomaterials with special morphology, synthesis of carbon peapods and DWCNT (double-walled carbon nanotubes).

List of Scientific Papers

- (1) Prochazka, J.; Kavan, L.; Shklover, V.; Zukalova, M.; Frank, O.; Kalbac, M.; Zukal, A.; Pelouchova, H.; Janda, P.; Mocek, K.; Klementova, M.; Carbone, D. *Chem. Mater.* **2008**, *accepted*,
- (2) Attia, A.; Zukalova, M.; Rathousky, J.; Zukal, A.; Kavan, L. *J. Solid State Electrochem.* **2005**, *9*, 138.
- (3) Attia, A.; Zukalova, M.; Pospisil, L.; Kavan, L. *J. Solid State Electrochem.* **2007**, *11*, 1163.
- (4) Frank, O.; Kalbac, M.; Kavan, L.; Zukalova, M.; Prochazka, J.; Klementova, M.; Dunsch, L. *Phys. Stat. Sol. (b)* **2007**, *244*, 4040.
- (5) Kalbac, M.; Zukalova, M.; Kavan, L. *J. Solid State Electrochem.* **2003**, *8*, 2.
- (6) Kalbac, M.; Kavan, L.; Zukalova, M.; Dunsch, L. *Carbon* **2004**, *42*, 2915.
- (7) Kalbac, M.; Kavan, L.; Kataura, H.; Zukalova, M.; Dunsch, L. In *Electronic Properties of Synthetic Nanostructures*; Kuzmany, H., Fink, J., Mehring, M., Roth, S., Eds.; AIP: New York, 2004; pp 242-246.
- (8) Kalbac, M.; Kavan, L.; Zukalova, M.; Dunsch, L. *J. Phys. Chem. B* **2004**, *108*, 6275.
- (9) Kalbac, M.; Kavan, L.; Juha, L.; Civis, S.; Zukalova, M.; Bittner, M.; Kubat, P.; Vorlicek, V.; Dunsch, L. *Carbon* **2005**, *43*, 1610.
- (10) Kalbac, M.; Kavan, L.; Zukalova, M.; Pelouchova, H.; Janda, P.; Dunsch, L. *Chemphyschem* **2005**, *6*, 426.
- (11) Kalbac, M.; Kavan, L.; Zukalova, M.; Dunsch, L. *Adv. Funct. Mater.* **2005**, *15*, 418.
- (12) Kalbac, M.; Kavan, L.; Pelouchova, H.; Janda, P.; Zukalova, M.; Dunsch, L. In *Electronic Properties of Novel Nanostructures*; Kuzmany, H., Fink, J., Mehring, M., Roth, S., Eds.; AIP: Melville, 2005; pp 65-68.
- (13) Kalbac, M.; Kavan, L.; Zukalova, M.; Dunsch, L. *Nano* **2006**, *1*, 219.
- (14) Kalbac, M.; Kavan, L.; Zukalova, M.; Dunsch, L. *Chemistry Eur. J.* **2006**, *12*, 4451.
- (15) Kalbac, M.; Kavan, L.; Zukalova, M.; Dunsch, L. *Phys. Stat. Sol. (b)* **2006**, *243*, 3134.

- (16) Kalbac, M.; Frank, O.; Kavan, L.; Zukalova, M.; Prochazka, J.; Klementova, M.; Dunsch, L. *J. Electrochem. Soc.* **2007**, *154*, K19-K24
- (17) Kalbac, M.; Kavan, L.; Zukalova, M.; Dunsch, L. *J. Phys. Chem. C* **2007**, *111*, 1079.
- (18) Kalbac, M.; Kavan, L.; Zukalova, M.; Yang, S.; Cech, J.; Roth, S.; Dunsch, L. *Chemistry Eur. J.* **2007**, *13*, 8811.
- (19) Kalbac, M.; Kavan, L.; Zukalova, M.; Dunsch, L. *Small* **2007**, *3*, 1746.
- (20) Kalbac, M.; Kavan, L.; Zukalova, M.; Dunsch, L. *Phys. Stat. Sol. (b)* **2007**, *244*, 4086.
- (21) Kalbac, M.; Kavan, L.; Zukalova, M.; Dunsch, L. *Carbon* **2007**, *45*, 1463.
- (22) Kavan, L.; Prochazka, J.; Spitler, T.M.; Kalbac, M.; Zukalova, M.; Drezen, T.; Grätzel, M. *J. Electrochem. Soc.* **2003**, *150*, A1000-A1007
- (23) Kavan, L.; Zukalova, M.; Kalbac, M.; Grätzel, M. *J. Electrochem. Soc.* **2004**, *151*, A1301-A1307
- (24) Kavan, L.; Kalbac, M.; Zukalova, M.; Exnar, I.; Lorenzen, V.; Nesper, R.; Grätzel, M. *Chem. Mater.* **2004**, *16*, 477.
- (25) Kavan, L.; Kalbac, M.; Zukalova, M.; Krause, M.; Kataura, H.; Dunsch, L. In *Electronic Properties of Synthetic Nanostructures*; Kuzmany, H., Fink, J., Mehring, M., Roth, S., Eds.; AIP: New York, 2004; pp 247-250.
- (26) Kavan, L.; Kalbac, M.; Zukalova, M.; Krause, M.; Dunsch, L. *Chemphyschem* **2004**, *5*, 274.
- (27) Kavan, L.; Kalbac, M.; Zukalova, M.; Dunsch, L. In *Physics, Chemistry and Application of Nanostructures*; Borisenko, V.E., Gaponenko, S.V., Gurin, V.S., Eds.; World Scientific Publ.: New Jersey, 2005; pp 55-61.
- (28) Kavan, L.; Kalbac, M.; Zukalova, M.; Dunsch, L. *J. Phys. Chem. B* **2005**, *109*, 19613.
- (29) Kavan, L.; Kalbac, M.; Zukalova, M.; Krause, M.; Dunsch, L.; Kataura, H. *Full. Nanotub. Carb. Nanostr.* **2005**, *13*, 115.
- (30) Kavan, L.; Kalbac, M.; Zukalova, M.; Dunsch, L. In *Electronic Properties of Novel Nanostructures*; Kuzmany, H., Fink, J., Mehring, M., Roth, S., Eds.; AIP: Melville, 2005; pp 309-312.
- (31) Kavan, L.; Kalbac, M.; Zukalova, M.; Dunsch, L. *Carbon* **2006**, *44*, 99.

- (32) Kavan, L.; Kalbac, M.; Zukalova, M.; Dunsch, L. *Phys. Stat. Sol. (b)* **2006**, *243*, 3130.
- (33) Kavan, L.; Zukalova, M.; Kalbac, M.; Osawa, E.; Dunsch, L. *Carbon* **2006**, *44*, 3113.
- (34) Kavan, L.; Kalbac, M.; Zukalova, M.; Dunsch, L. *Phys. Rev. Lett.* **2007**, *98*, 019701
- (35) Tarabek, J.; Kavan, L.; Kalbac, M.; Rapta, P.; Zukalova, M.; Dunsch, L. *Carbon* **2006**, *44*, 2147.
- (36) Zukalova, M.; Kalbac, M.; Kavan, L. In *Nanoengineered Assemblies and Advanced Micro/Nanosystems Proceedings*; Taylor, D.P., Liu, J., McIlroy, D., Merhari, L., Pendry, J.B., Borenstein, J.T., Eds.; MRS: Warrendale, 2004; pp R531-R536
- (37) Zukalova, M.; Kalbac, M.; Kavan, L.; Exnar, I.; Haeger, A.; Grätzel, M. *Prog. Solid St. Chem.* **2005**, *33*, 253.
- (38) Zukalova, M.; Kalbac, M.; Kavan, L.; Exnar, I.; Grätzel, M. *Chem. Mater.* **2005**, *17*, 1248.
- (39) Zukalova, M.; Zukal, A.; Kavan, L.; Nazeeruddin, M.K.; Liska, P.; Grätzel, M. *Nano Lett.* **2005**, *5*, 1789.
- (40) Zukalova, M., Kalbac, M., Kavan, L., and Exnar, I. Energy Storage Device. (WO 2006/033069 A2). 2006.
- (41) Zukalova, M.; Prochazka, J.; Zukal, A.; Yum, J.H.; Kavan, L. *Inorg. Chim. Acta* **2008**, *361*, 656.
- (42) Zukalova, M.; Rathousky, J.; Zukal, A. *Coll. Czech. Chem. Commun.* **2003**, *68*, 2019.
- (43) Rathousky, J.; Zukalova, M.; Zukal, A. *Coll. Czech. Chem. Commun.* **1998**, *63*, 271.
- (44) Rathousky, J.; Zukalova, M.; Zukal, A.; Had, J. *Coll. Czech. Chem. Commun.* **1998**, *63*, 1893.
- (45) Rathousky, J.; Zukalova, M.; Zukal, A. *Chem. listy* **1997**, *91*, 413.
- (46) Krylova, A.Y.; Lapidus, A.L.; Sominskii, S.D.; Rar, L.F.; Zukal, A.; Ratkousky, J.; Jancalkova, M.; Yakerson, V.I. *Bulletin of the Russian Academy of Sciences-Division of Chemical Science* **1992**, *41*, 41.
- (47) Lapidus, A.; Krylova, A.; Rathousky, J.; Zukal, A.; Jancalkova, M. *Applied Catalysis A-General* **1992**, *80*, 1.

- (48) Lapidus, A.; Krylova, A.; Rathousky, J.; Zukal, A.; Jancalkova, M. *Journal of Molecular Catalysis* **1992**, *71*, 183.
- (49) Lapidus, A.; Krylova, A.; Kazanskii, V.; Borovkov, V.; Zaitsev, A.; Rathousky, J.; Zukal, A.; Jancalkova, M. *Applied Catalysis* **1991**, *73*, 65.
- (50) Vohlidal, J.; Hollander, A.; Jancalkova, M.; Sedlacek, J.; Sargankova, I. *Coll. Czech. Chem. Commun.* **1991**, *56*, 351.